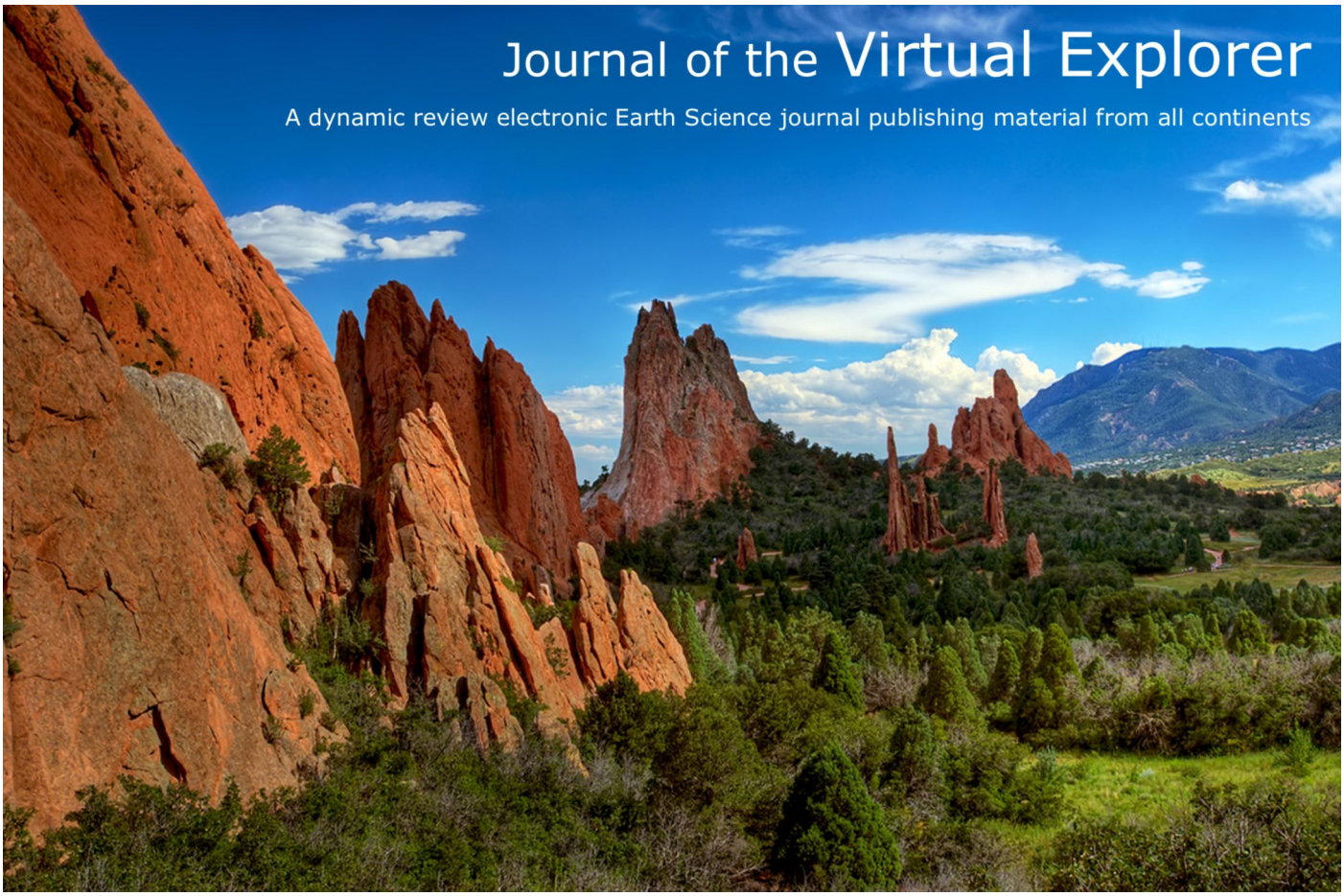

Using multiscale structural analysis to infer high-/ultrahigh-pressure assemblages in subducted rodingites of the Zermatt-Saas Zone at Valtournanche, Italy

Davide Zanoni, Gisella Rebay, Jacopo Bernardoni, Maria Iole Spalla

Journal of the Virtual Explorer, Electronic Edition, ISSN 1441-8142, volume **41**, paper 6
In: (Eds.) Michele Zucali, Maria Iole Spalla, and Guido Gosso,
Multiscale structures and tectonic trajectories in active margins, 2012.

Journal of the Virtual Explorer, 2012
Volume 41
Paper 6
http://virtualexplorer.com.au/

Using multiscale structural analysis to infer high-/ultrahigh-pressure assemblages in subducted rodingites of the Zermatt-Saas Zone at Valtournanche, Italy

Davide Zanoni
Dipartimento di Scienze della Terra "A. Desio", Università degli Studi di Milano, via Mangiagalli, 34, 20133 Milano, Italy. *Email: davide.zanoni@unimi.it*

Gisella Rebay
Dipartimento di Scienze della Terra e dell'Ambiente, Università degli Studi di Pavia, via Ferrata, 1, 27100 Pavia, Italy. *Email: gisella.rebay@unipv.it*

Jacopo Bernardoni
Dipartimento di Scienze della Terra "A. Desio", Università degli Studi di Milano, via Mangiagalli, 34, 20133 Milano, Italy.

Maria Iole Spalla
1. Dipartimento di Scienze della Terra "A. Desio", Università degli Studi di Milano, via Mangiagalli, 34, 20133 Milano, Italy.
2. CNR-IDPA, via Mangiagalli, 34, 20133 Milano, Italy.

Abstract: Rodingites hosted in serpentinites of the upper Valtournanche (Zermatt-Saas Zone) record four stages of ductile deformation of which the first three are associated with new mineral growth; D_1 and D_2 developed under high-pressure to ultrahigh-pressure conditions and D_3 under lower pressure conditions.

On the base of the modal amount of the main mineral phases three types of rodingites are individuated: epidote-, garnet-chlorite-clinopyroxene-, and vesuvianite-bearing rodingites. They are interpreted as deriving from ocean floor metasomatism of former gabbro dykes intruded in mantle rocks, successively affected by subduction-related metamorphism during the Alpine convergence.

Field mapping allowing continuous structural correlation shows that the deformation history recorded in the serpentinites affects also rodingites. On the basis of syn-D_2 peak conditions already inferred in serpentinites (2.5 ± 0.3 GPa and 600 ± 20 °C) the following syn-D_2 assemblages in rodingites are interpreted as developed under the same physical conditions, during the Alpine subduction: epidote$_{II}$, clinopyroxene$_{II}$, Mg-chlorite$_{II}$, titanite$_I$, ± garnet$_{II}$, ± tremolite$_I$ in epidote-bearing rodingites; Mg-chlorite$_{II}$, garnet$_{II}$, clinopyroxene$_{II}$, ± vesuvianite$_{II}$, ± opaque minerals, in garnet-chlorite-clinopyroxene-bearing rodingites; vesuvianite$_{II}$, Mg-chlorite$_{II}$, clinopyroxene$_{II}$, garnet$_{II}$, ± titanite$_I$, ± epidote$_I$ in vesuvianite-bearing rodingites. Pre-D_1 mineral relicts such as Cr-rich spinel and cm-sized clinopyroxene porphyroclasts are interpreted as magmatic vestiges of the rodingitised and eclogitised gabbro dykes, whereas Cr-rich garnet and Cr-Ti-Ca-rich vesuvianite as developed during oceanic metasomatism. Distinct chemical compositions characterise the same minerals recrystallised during the Alpine subduction. Finally, multiscale structural analysis shows that the dominant structural and metamorphic imprint recorded by the Valtournanche eclogitised rodingites developed during the Alpine subduction and that, in the favourable bulk composition (Ca-rich), vesuvianite is stable also at metamorphic conditions close to ultrahigh-pressure.

Citation: 2012. Using multiscale structural analysis to infer high-/ultrahigh-pressure assemblages in subducted rodingites of the Zermatt-Saas Zone at Valtournanche, Italy. In: (Eds.) Michele Zucali, Maria Iole Spalla, and Guido Gosso, *Journal of the Virtual Explorer*, volume **41**, paper 6, doi: 10.3809/jvirtex.2011.00290

Introduction

The origin of rodingites contained within serpentinite massifs is generally considered as a side effect of serpentinisation of mantle rocks (e.g. O'Hanley *et al.*, 1992) taking place mostly in the ocean floor environment. During this process, metasomatic fluids, enriched in Ca^{2+} (e.g. Honnorez & Kirst, 1975; Nicolas, 1966) by the destabilisation of clinopyroxene (e.g. Austrheim & Prestvik, 2008; Coleman, 1967), drive the transformation of mafic dykes, emplaced in mantle rocks, into Si-undersaturated and Ca-rich rodingites.

Even if rodingitisation may also take place in subduction environments, as in the case of the Othrys massif (Tsikouras *et al.*, 2009), most of the models consider rodingitisation to be a metasomatic ocean floor process (e.g. Bach & Klein, 2009; Palandri & Reed, 2004; Panseri *et al.*, 2008). Geochemical analyses from the present ocean floor support this last model (e.g. Frost *et al.*, 2008). Therefore, metamorphic transformations involving rodingites during the evolution of a convergent system are generally neglected, except modelling at pressure ≤ 1 GPa (Castelli *et al.*, 1995; Rice, 1983) or studies on the effects of contact metamorphism on rodingites (Frost, 1975).

The earlier authors, who investigated rodingites in the orogenic environment of the Alpine belt (Amstutz, 1962; Cornelius, 1912; Rondolino, 1937; Staub, 1915; Weinschenk, 1894), described mineral assemblages of these rocks as metasomatic relicts unaffected by regional metamorphism. Later Dal Piaz (1967) pointed out that rodingites were widely re-equilibrated during their Alpine high-pressure (HP) evolution together with their country rocks. In addition, rodingites affected by HP metamorphism have been described in the Voltri massif (Messiga *et al.*, 1983; Piccardo *et al.*, 1980) in the Mulhacén complex of Southern Spain (Puga *et al.*, 1999), and in the Pfulwe region and south of the Aosta-Ranzola fault in the Zermatt-Saas Zone (Ferrando *et al.*, 2010; Li *et al.*, 2008).

In order to define the HP mineral assemblages in the boudinaged rodingites of the Valtournanche area, embodied in HP/ultrahigh pressure (UHP) partly de-hydrated serpentinites of Zermatt-Saas Zone (Rebay *et al.*, 2012), we undertook a multiscale analysis to recognize the combined structural and metamorphic evolution of these rocks.

Relationships between deformation and metamorphism have been used as a tool to carry out structural correlation in metamorphic terrains (e.g. Hobbs *et al.*, 2010; Pitcher & Flinn, 1965; Turner & Weiss, 1963; Williams, 1985) and in recent times also to define shape and size of tectono-metamorphic units in orogenic belts (e.g. Spalla *et al.*, 2000; 2005). We used multiscale structural analysis to individuate stable mineral assemblages marking superposed fabrics developed during multistage deformation in rodingites. Correlation among superposed structures affecting rodingites, hosting serpentinites, and associated metagabbros is based on a structural mapping, performed at 1:5,000 scale. The deformation history provides the reference frame to ensure a meaningful correlation of mineral assemblages in rocks with different bulk compositions; a detailed microstructural analysis on fabrics scaled in time validates the relative chronology at the regional scale. Furthermore, we took advantage of the already acquired knowledge on the thermodynamic constraints on mineral phase stability for chemical systems characterising ultramafic and mafic rocks and of numerous studies on the HP metamorphic conditions of the Zermatt-Saas Zone to infer the HP/UHP mineral assemblages developed in rodingite.

Mineral abbreviations in the text and figures are according to Whitney and Evans (2010).

Geological setting

Zermatt-Saas and Combin zones (ZSZ and CZ) consist of fragments of mantle and crustal rocks of the Piemonte-Ligurian ocean, marking the suture zone of the Western European Alps (Caron *et al.*, 1984; Reddy *et al.*, 1999; Spalla *et al.*, 2010 and refs therein). These two zones tectonically overlie the continental Monte Rosa and underlie the Dent Blanche – Sesia Lanzo nappes, which belong, respectively, to the Penninic and Austroalpine domains (e.g. Bearth, 1967; Polino *et al.*, 1990). The ZSZ (Fig. 1) is structurally beneath the CZ. Because of the different lithostratigraphic and metamorphic features these two units seem to derive, respectively, from the oceanic lithosphere and from the ocean-continent transition zone. The Pancherot – Cime Bianche unit, consisting of metasediments deriving from Permian to Cretaceous protholits, and slices of pre-Alpine continental rocks separate ZSZ and CZ (Dal Piaz, 1999).

Figure 1. Geological map of the upper Valtournanche

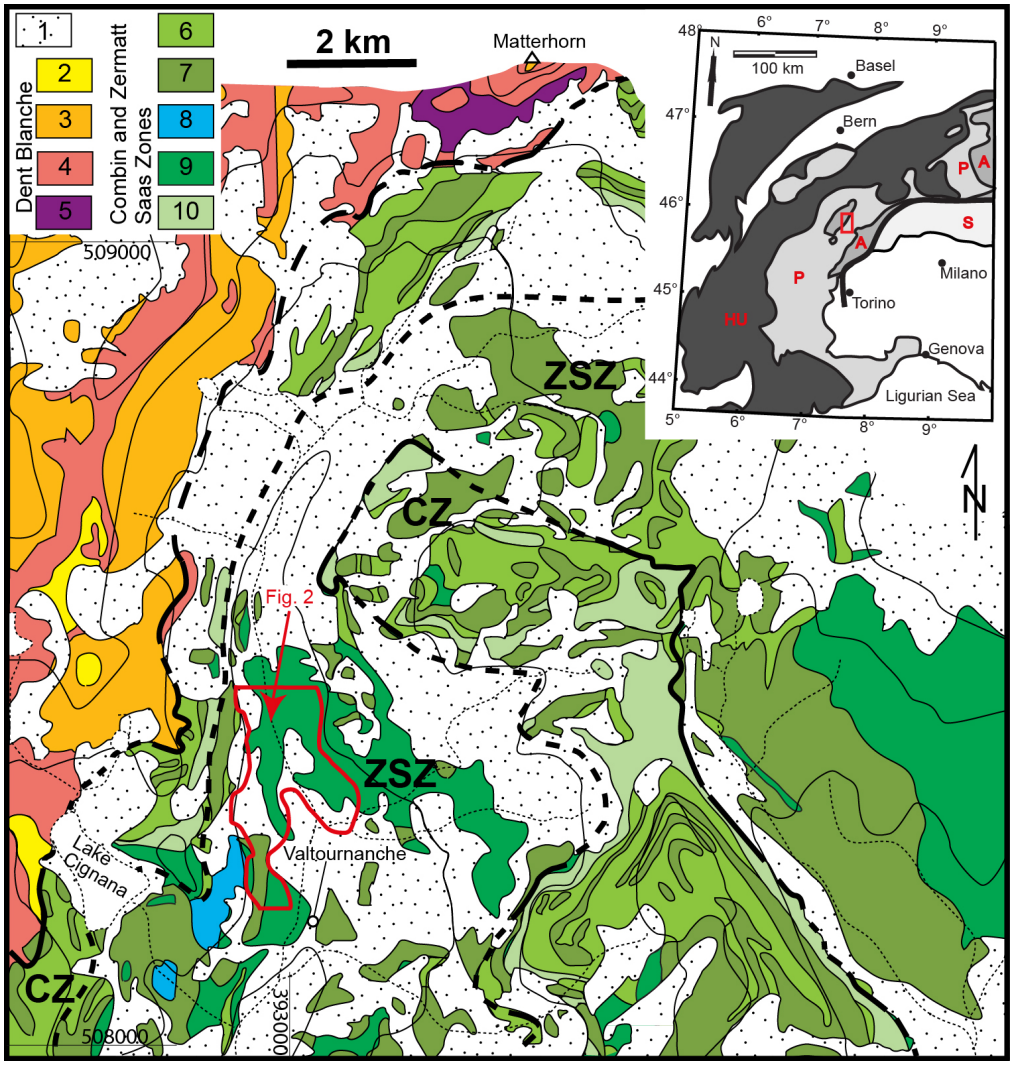

ZSZ = Zermatt - Saas Zone; CZ = Combin Zone. 1 = undifferentiated Quaternary deposits; Austroalpine Domain: 2 = Mesozoic covers; 3 = Kinzigitic complex; 4 = Fine-grained metagranitoids and paraschists; 5 = Permian gabbros; Penninic Domain: 6 = Calcschists; 7 = Prasinites, amphibolites and minor eclogites; 8 = Meta-gabbros; 9 = Serpentinites; 10 = Undifferentiated Permian-Mesozoic covers. In the inset the tectonic sketch map of the Western Alps: HU = Helvetic and Ultrahelvetic Domain; P = Penninic Domain and Pre-Alps; A = Austroalpine Domain; S = Southalpine Domain. Thick red line delimitates the map of Fig. 2. Map redrawn after De Giusti *et al.* (2003).

Despite the pervasive greenschist facies metamorphism, CZ rocks preserve blueschist facies relicts, whereas remnants of eclogite facies assemblages are not documented even in the less deformed rocks (Cartwright & Barnicoat, 2002; Dal Piaz, 1974; Dal Piaz & Ernst, 1978; Ring, 1995).

The ZSZ consists of serpentinites, metagabbros, and N-MORB metabasalts with minor pelagic metasediments (Beccaluva *et al.*, 1984; Dal Piaz *et al.*, 1981; Pfeiffer *et al.*, 1989; Rebay *et al.*, 2012); metasediments are mainly calcschists and quartzites deriving from the internal part of the oceanic realm (e.g. Bearth, 1967; Ernst & Dal Piaz, 1978).

The Alpine subduction-related eclogite facies imprint is the dominant one in the ZSZ and is partly obliterated by exhumation-related greenschist facies metamorphism (e.g. Cartwright & Barnicoat, 2002; Ernst & Dal Piaz, 1978). The PT evolution of the ZSZ is characterised by a prograde path under blueschist facies predating eclogite facies conditions (e.g. Chinner & Dixon, 1973; Ernst & Dal Piaz, 1978). Generally the eclogite facies imprint reveals conditions up to about 3.0 GPa. In detail recent

petrological investigations on ZSZ metabasic rocks (from Saas-Fee) indicate pressure around 2.5-3.0 GPa, for temperatures of 550-600°C (Bucher *et al.*, 2005), whereas on the Allalin gabbro indicate 2.5-2.8 GPa and 600- 610°C (Bucher & Grapes, 2009). Highest pressure conditions from 2.7 to higher than 3.2 GPa for temperatures between 590 and 630°C are estimated at Lago di Cignana, which is considered a separate unit (e.g. Groppo *et al.*, 2009; Reinecke, 1991; Reinecke, 1998; Van der Klauw *et al.*, 1997), and in which recently microdiamonds inclusions have been detected in oceanic metasediments (Frezzotti *et al.*, 2011). In the portion of ZSZ south of the Aosta-Ranzola fault (St. Marcel valley) different PT-peak conditions of 2.1±0.3 GPa and 550±60°C have been inferred in metabasics (Martin *et al.*, 2008). HP conditions are also estimated in serpentinites at 2.0-2.5 GPa for temperature of 600-650°C and at 2.2-2.8 GPa for 580-620°C in the northern part of the ZSZ (Li *et al.*, 2004b) and at Valtournanche (Rebay *et al.*, 2012) respectively. In the Zermatt area PT-peak conditions proposed for metarodingites (Li *et al.*, 2008), on the base of coherence between petrologic modelling of rodingites and PT evolution inferred from surrounding metabasic rocks, suggest PT values of 2.5-2.8 GPa and 600-625°C (Bucher *et al.*, 2005).

The peak-conditions and the related PT trajectories reconstructed all over the ZSZ indicate that the metamorphic evolution of this complex has been heterogeneous, even though some authors, after petrologic investigations on metabasic rocks and calcschists, suggested a homogeneous metamorphic evolution for the entire ZSZ, characterised by PT peak conditions of 2.3 ± 0.1 GPa and 540 ± 40°C (Angiboust & Agard, 2010; Angiboust *et al.*, 2009).

Oceanic relict textures are well documented in the ZSZ (Barnicoat & Fry, 1986; Fontana *et al.*, 2008; Martin & Tartarotti, 1989) and the age of these relics ranges between 164 and 153 Ma (Rubatto, 1998). Pre-Alpine structural and mineral relics show that this lithosphere was variously affected by oceanic metamorphism before the Alpine subduction (Bearth, 1976; Dal Piaz *et al.*, 1980; Li *et al.*, 2004a).

As already described in the upper Valtournanche (Dal Piaz, 1965; 1967; 1969), rodingites of the Western Alps are interpreted as former gabbro dykes likely recrystallised during the four Alpine ductile deformation stages affecting the hosting serpentinites (Dal Piaz *et al.*, 1980). Clinopyroxene porphyroclasts with igneous composition are the only mineral relics of the gabbro protolith (Dal Piaz *et al.*, 1980; Li *et al.*, 2004a).

In the Lanzo Massif rodingites derive from gabbro dykes (Bortolami & Dal Piaz, 1968; Dal Piaz, 1969) metasomatised by Cretaceous seawater and subsequently subducted with the hosting serpentinites during the Alpine convergence (Rösli *et al.*, 1991). However late Alpine multi-stage rodingitisation has been described in the Balangero mine of the Lanzo Massif (Castelli *et al.*, 1995), as well as at Bellecombe in the ZSZ, where late greenschist Alpine metasomatism took place, but high-pressure Alpine minerals also occur in rodingites (Ferrando *et al.*, 2010). Finally, a recent petrological work on rodingites from the Zermatt area shows that their main mineral assemblages formed during the Alpine subduction (Li *et al.*, 2008).

In the ZSZ different type of rodingite, mainly distinguished on the basis of their mineral content (Panseri *et al.*, 2008), are ascribed to different protoliths or degrees of metasomatic transformation (Li *et al.*, 2004a). Li *et al.* (2008) interpret the potential Alpine assemblages exclusively on the basis of consistency between thermodynamic modelling for these rocks and PT evolution constrained in ZSZ metabasic rocks. However their modelling allow identifying near-isothermal reactions in rodingites and they do not describe any structural correlation with superposed fabrics marked by eclogite and greenschist facies minerals in the hosting eclogitised ophiolites.

Deformation history

Structural mapping has been performed in an area of the upper Valtournanche valley, where the local bedrocks are mostly serpentinites and metagabbros, with minor prasinites, calcschists, and rodingites (Fig. 2). Here outcrops are continuous, allowing walking correlation of superposed structures and continuous structural mapping to realize a detailed foliation trajectory map and cross sections up to *ca.* 2 km long, on which relationships between superposed fabric elements are reported.

Figure 2. Foliation trajectory map with interpreted lithostratigraphy of the meta-ophiolites of the upper Valtournanche (ZSZ).

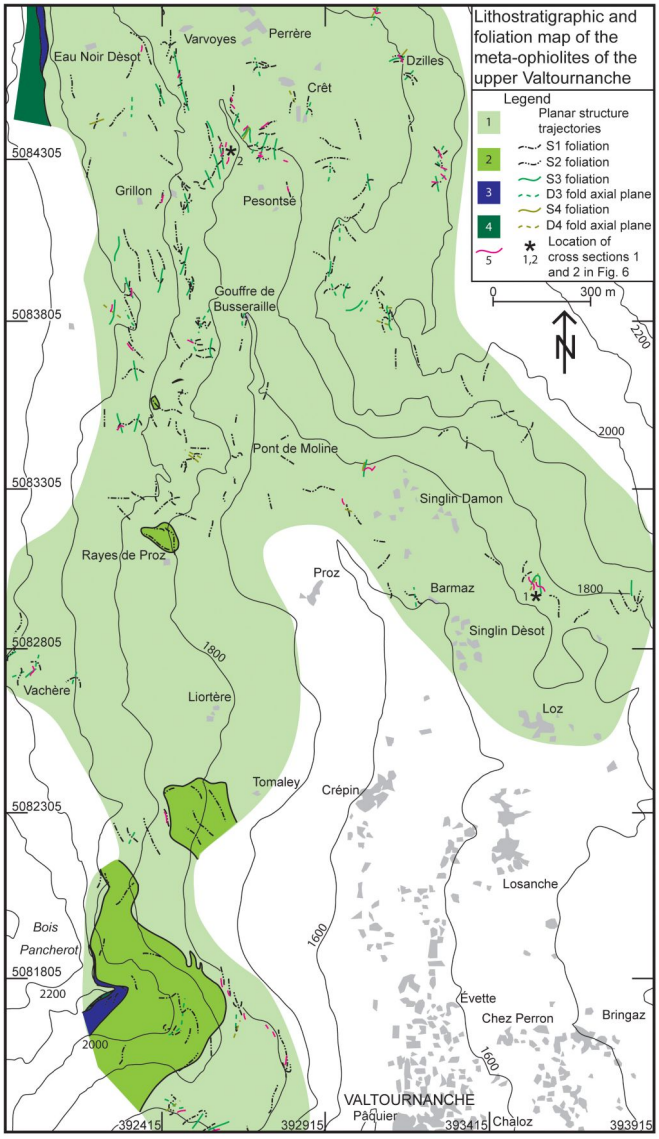

Legend: 1 = serpentinites; 2 = metagabbros and minor amphibolites; 3 = calcschists; 4 = prasinites; 5 = rodingites. Topography redrawn from the technical map of Val d'Aosta Regional Administration. No hydrography is indicated. UTM coordinate system, map datum ED50, zone 32N. *1 and *2 are the locations of detailed structural sections of Fig. 6.

Here, four main ductile deformation stages (D_1, D_2, D_3, and D_4) have been recorded in serpentinites, metagabbros, and rodingites. The first three stages produce a foliation supported by distinctive metamorphic assemblages and mineral compositions in serpentinite (Rebay *et al.*, 2012), whereas the last one is mainly responsible for open folds and a very localised disjunctive cleavage (Passchier & Trouw, 2005). The main structural feature of the area is the S_1/S_2 composite foliation, generally well developed in the serpentinites. S_1 and S_2 foliations can be distinguished only where they are superposed; in this case S_2 occurs as a crenulation cleavage of S_1.

- D_1: S_1 is a continuous sub-vertical foliation dipping mainly toward WSW and to a lesser extent toward ENE, because it has been dispersed by D_2 folding (Fig. 3). The maximum concentration of S_1/S_2 composite foliation poles is consistent with that of S_2 poles. Only locally S_1 is dominant with respect to S_2 (Fig. 4a).

Figure 3. Plots of the structural data

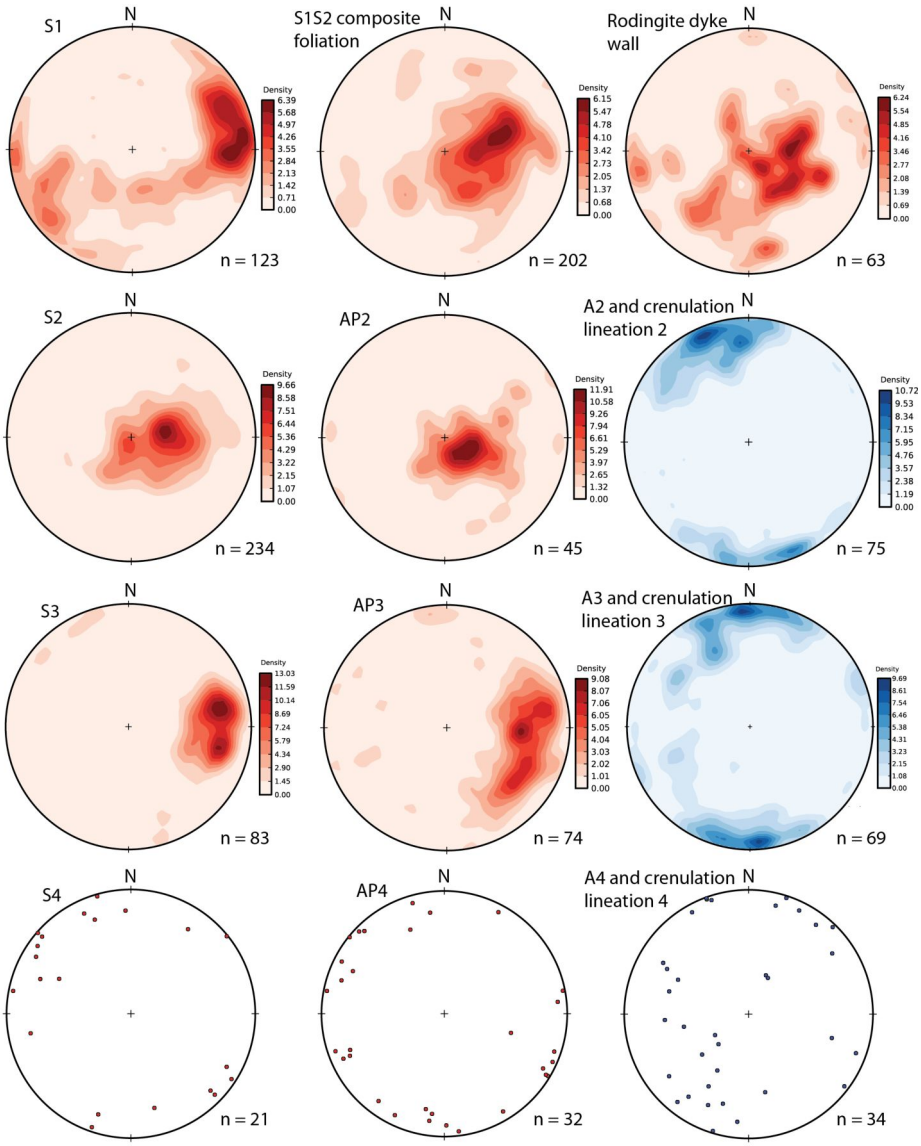

Density plots of linear (blue) and planar (red) structural data for foliations, fold axial planes, fold axes, and crenulation lineations of ductile structures in serpentinites, metagabbros, and rodingites.For D_4 structures, pole to plane scattered plots are shown. Lower hemisphere, Schmidt equal area projection. “n” = number of data.

Figure 4. Structures in serpentinites

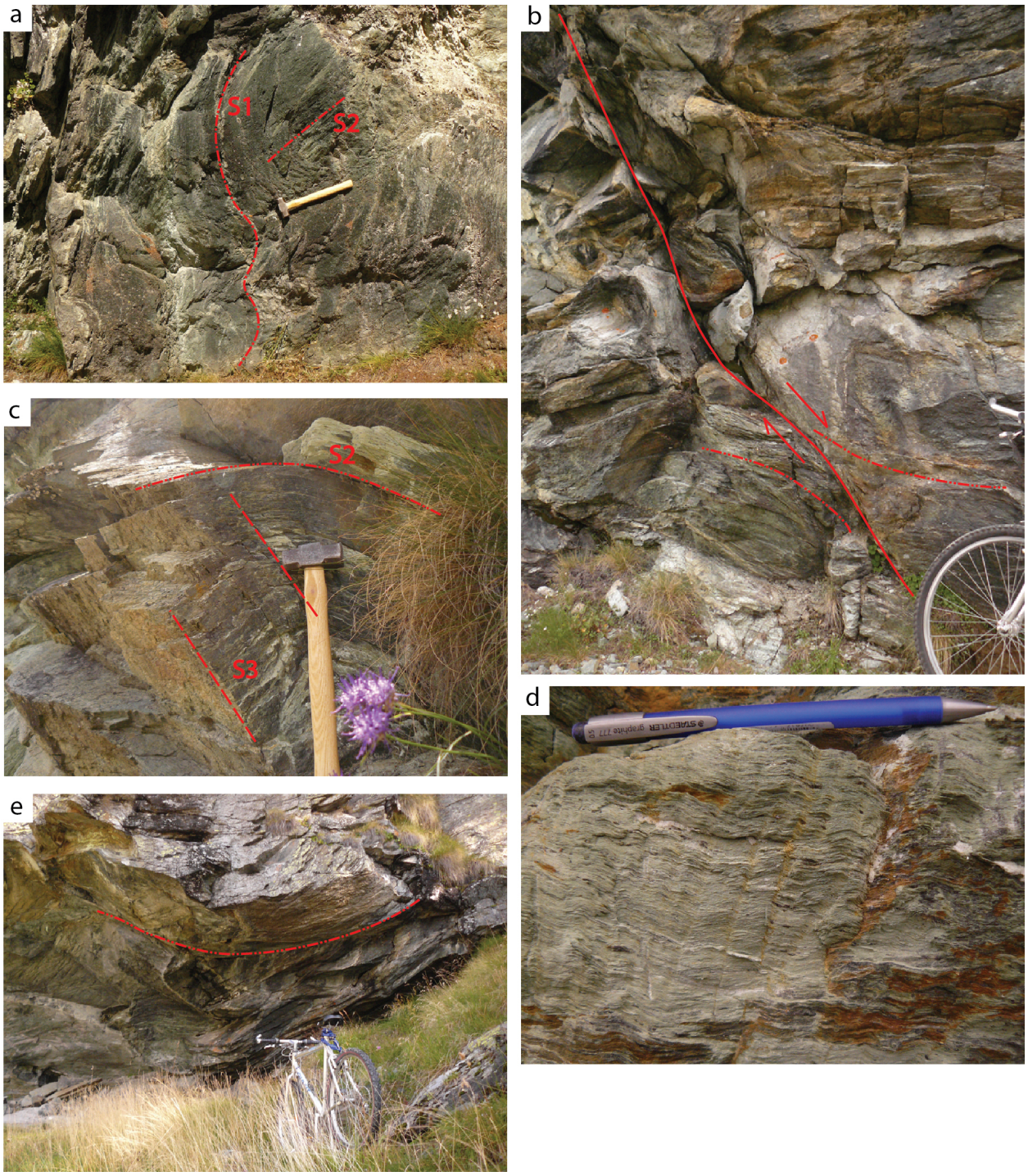

a) Pervasive S_1 in serpentinites folded by D_2 associated with an S_2 crenulation cleavage. West of Gouffre de Busseraille; b) Late D_2 normal shear zone in serpentinites west of Pesontsé. c) S_3 disjunctive cleavage overprinting S_2 in serpentinites, close to Varvoyes. d) S_3 crenulation cleavage in serpentinites in the Bois Pancherot area. e) D_4 folding of S_2 in the serpentinites north of Pesontsé.

- D_2: This group of structures mainly consists of up to metric folds, S_2 foliation, AP_2 fold axial plane, A_2 fold axis, and L_2 crenulation lineation. D_2 folds are from open to isoclinal, generally associated with an axial plane foliation (S_2) that is sub-horizontal and gently dipping to the W (Fig. 4a). The orientation of S_2 is not very dispersed,

because both D_3 and D_4 deformation stages produce a gentle folding (Fig. 3). AP_2 fold axial planes gently dip to the WNW and L_2 crenulation lineation and A_2 fold axis shallowly plunge to the NNW or SSE (Fig. 3). Late D_2 shear zones accommodate mainly a normal shearing, dip about 45° to the WNW (Fig. 4b) and locally are overprinted by D_3 folds.

- D_3: D_3 metric folds are open (Fig. 4c) to tight. In average, the fold axial plane dips 50-70° to the W and both the fold axis and the crenulation lineation gently plunge to the N or S (Fig. 3). The S_3 crenulation foliation (Fig. 4d) generally dips 60-70° to the W (Fig. 3) and locally is a disjunctive cleavage (Fig. 4c).

- D_4: D_4 mainly produces upright open folds (Fig. 4e), of metric size, and a rare S_4 disjunctive cleavage develops in serpentinites. D_4 produces open to tight cm-sized folds in well-foliated serpentinite. S_4 and D_4 axial planes are sub-vertical and generally trend NE – SW. D_4 fold axes and crenulation lineations are mainly shallowly trending NNW – SSE (Fig. 3).

Structural correlation between serpentinite and rodingite dykes

The foliation trajectory map (Fig. 2) constitutes the chronological reference frame for the relative timing of foliation development; grids of successive foliations transecting lithologic boundaries played a relevant role for the correlation of mineral assemblages within different bulk chemistry (e.g. rodingites and serpentinites), since the whole deformation history is recorded both in serpentinites and their rodingitised gabbro dykes.

The orientation of rodingite dykes is mainly parallel to the pervasive S_2 or composite S_1/S_2 foliations (Fig. 3), as dykes are transposed into these foliation attitudes. Usually the dominant structure in the dykes is the S_2 foliation, which is physically continuous from serpentinites to rodingites (Figs. 5a, b). Only locally rodingites record an S_1 foliation that can be overprinted by an S_2 crenulation foliation (Fig. 5c). Late-D_2 shear zones affect the margin of rodingite dykes (Fig. 5d). Locally D_3 is responsible for an intense folding of the dykes producing an S_3 crenulation cleavage that from serpentinites extends into rodingites or affects only the reaction rims between the two rock types (Fig. 5e). D_4 may be sporadically responsible for a gentle folding of the dykes. Generally, structures extending from serpentinites to rodingites can be continuously followed and correlated along outcrops up to about 50 m long and the regional scale correlation is supported by the 1:5,000 scale mapping, synthesised in Fig. 2. Significant examples are the detailed structural sections on the slopes above Singlin Dèsot and Pesontsé (*1 and *2 respectively in Fig. 6), whose location is shown on the map of Fig. 2. The stereoplots on Fig. 6 show that orientation data of planar and linear structures in serpentinite are coherent with those in rodingites.

Figure 5. Structures affecting serpentinite and rodingite

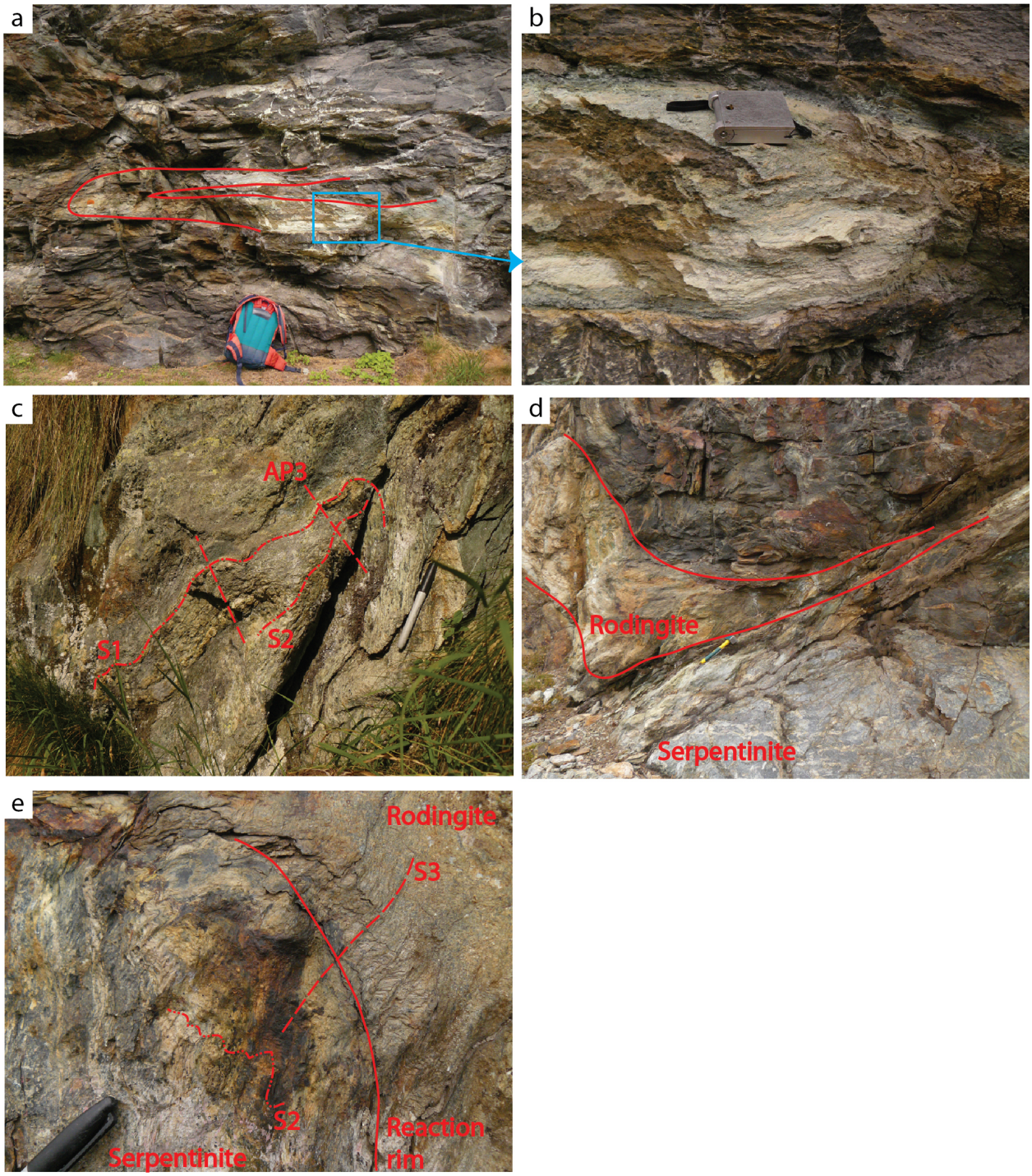

a) Rodingite dyke isoclinally folded by D_2. North of Pesontsé. b) Close up showing the pervasive S_2 foliation continuous from serpentinite to rodingite. c) S_1 in rodingite dyke overprinted by S_2 and folded by D_3. South of Dzilles. d) Late-D_2 normal shear zone involving a rodingite dyke. Slope above Singlin Dèsot. e) Refracted S_3 crenulation cleavage across serpentinite - rodingite reaction rim. S_3 is not recorded in the rodingite dyke core. Slope above Singlin Dèsot.

Figure 6. The shared structural history of serpentinites and rodingites

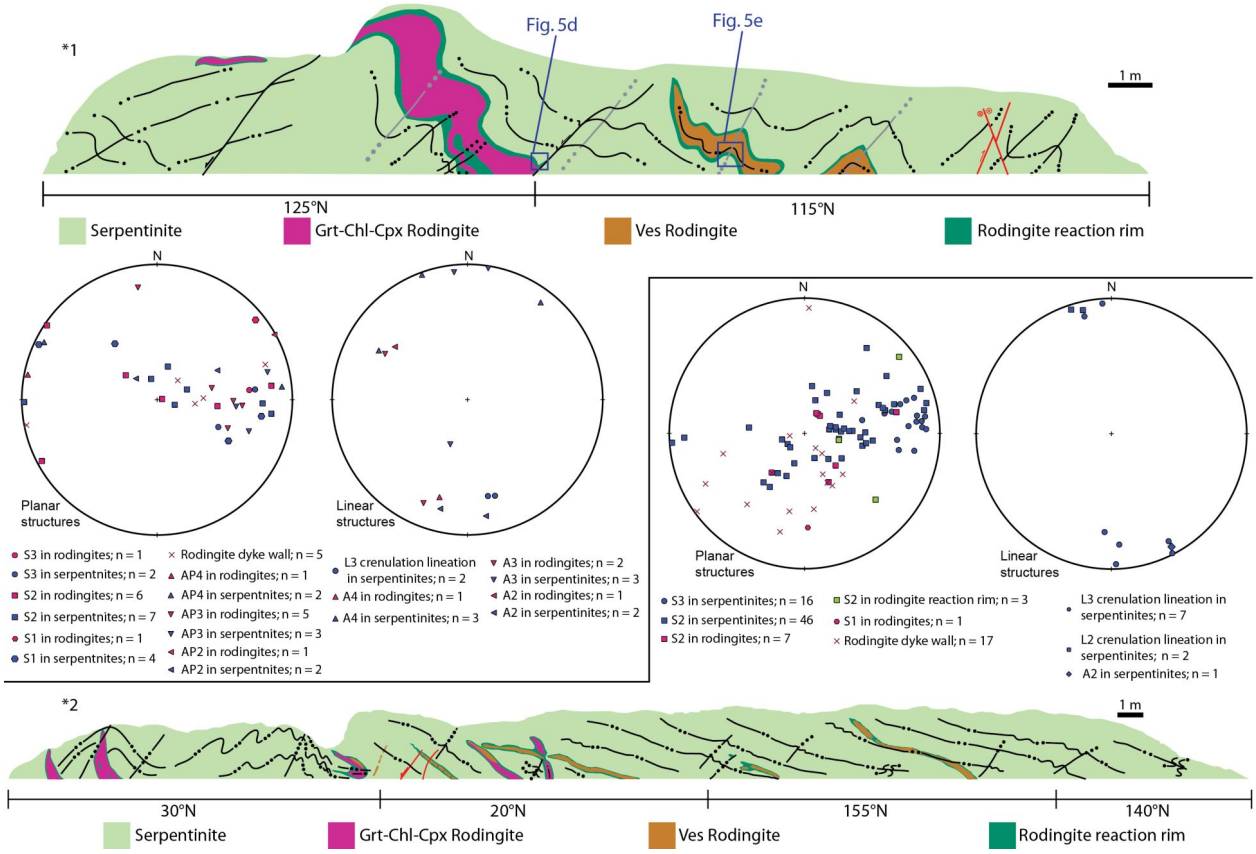

Natural structural cross-sections *1 and *2 (located in the regional scale map of Fig. 2) objectively showing close ups of the common structural history of serpentinites and rodingites. Lower hemisphere equal area stereo plots report in detail the orientation data of planar and linear structures. Foliation trajectories and fold axial plane traces are in black and grey respectively, with 1, 2 or 3 dots indicating their relative chronology. The position of the field photos (Figs. 5d and 5e) is indicated in the cross-section *1.

Microstructures of rodingites

Three types of rodingites have been distinguished on the basis of their main mineral constituents, epidote, garnet, clinopyroxene, chlorite and vesuvianite.

Epidote-bearing rodingites consist of whitish layers of epidote and greenish layers of clinopyroxene, locally containing mm-sized greenish chlorite lenses. Up to cm-sized grey to pale green clinopyroxene porphyroclasts occur, whereas vesuvianite is absent.

Garnet-chlorite-clinopyroxene-bearing rodingites are pale pink to red or rarely green rocks, whose foliation is defined by up to 1 or 2 cm-thick chlorite- and garnet-rich layers. Whitish grey aggregates of clinopyroxene and rare epidote and garnet are parallel to the foliation. Clinopyroxene porphyroclasts show a grey violet colour and are up to 5 cm-sized (Fig. 7). Bright green aggregates made of Cr-garnet and spinel may occur. Vesuvianite + epidote never exceed 10% in volume.

Figure 7. Relict magmatic texture in rodingites

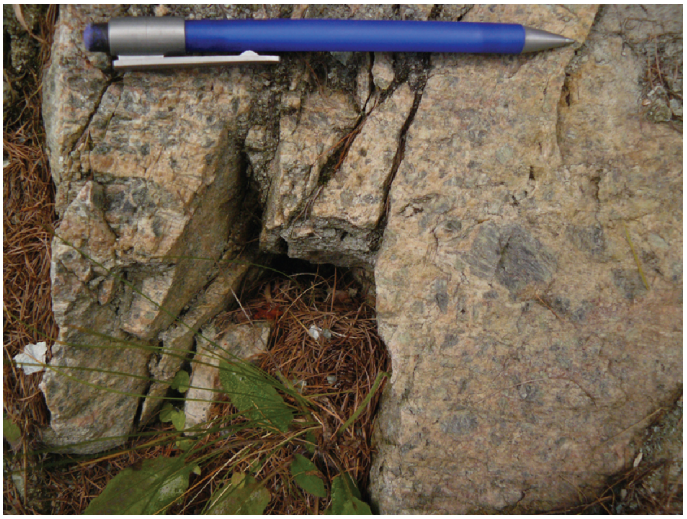

Cm-sized clinopyroxene porphyroclasts in a rodingite boudin south of Crépin, close to the contact with metagabbros. The composite S_1/S_2 foliation wraps the porphyroclasts.

Vesuvianite-bearing rodingites are characterised by a micro-crystalline green matrix consisting of chlorite, garnet, and clinopyroxene in variable proportions. Locally there are cm-sized clinopyroxene porphyroclasts aligned parallel to the composite S_1/S_2 foliation. In places garnet- and calcite-bearing veins are positioned at a high angle to boudin elongation.

Epidote-bearing rodingites

The main mineral phases are: epidote (20 - 70%), clinopyroxene (15 - 50%), Mg-chlorite (10 - 20%), garnet ($\leq$ 20%), tremolite ($\leq$ 5%).

S_1 foliation is defined by SPO (Shape Preferred Orientation) of epidote$_I$ and by LPO (Lattice Preferred Orientation) of Mg-chlorite$_I$ and clinopyroxene$_I$. Epidote$_I$ (locally Fe-epidote) forms euhedral zoned, coarse-grained, and twinned crystals. Garnet$_I$ is enclosed in, and shows rational rims with epidote$_I$ (Fig. 8a). Clinopyroxene$_I$ and minor epidote$_I$ form aggregates parallel to S_1. The margins of clinopyroxene$_I$ show inclusion trails marked by opaque minerals in continuity with, and sub-parallel to the external S_1.

Figure 8. Pre-Alpine and Alpine microstructures in Epidote-bearing rodingites.

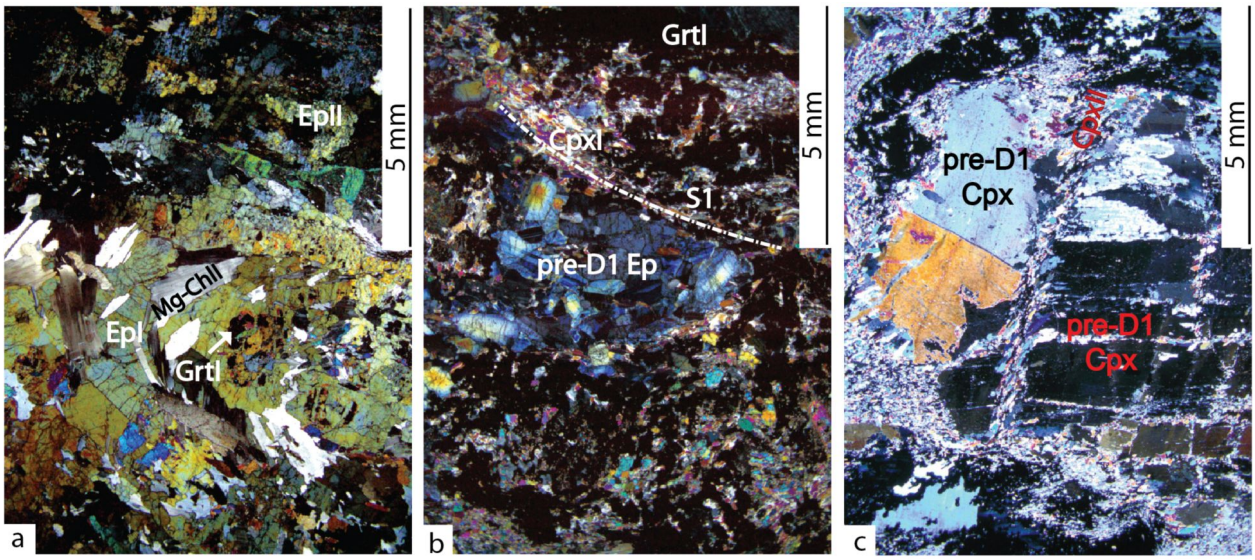

Mineral compositions related to microstructural sites are shown in Figs. 12, 13, and 14 and in Tables 1 and 2. a) D_2 folding deforms Mg-chlorite$_I$ and epidote$_I$ that dynamically recrystallise. Garnet$_I$ is enclosed in epidote$_I$. b) S_1 foliation, marked by Mg-chlorite$_I$, garnet$_I$, and clinopyroxene$_I$, wraps around an epidote aggregate. Crossed polars. c) clinopyroxene$_{II}$ in the fractures and along cleavages of a Pre-D_1 clinopyroxene porphyroclast. Crystal-plastic shear deformation is accommodated in clinopyroxene$_{II}$, garnet$_{II}$, and minor tremolite$_I$ multi-granular aggregate filling fractures. Crossed polars.

S_2 is defined by SPO and/or LPO of clinopyroxene$_{II}$, garnet$_{II}$, Mg-chlorite$_{II}$, epidote$_{II}$, and rare tremolite$_I$. Epidote$_{II}$, often forming polygonal aggregates, is also enclosed in Mg-chlorite$_{II}$. Veins consisting of pre-D_2 garnet

and minor pre-D_2 epidote are folded by D_2 and may be locally transposed into the folded S_1. Mg-chlorite$_I$ forms porphyroclasts within S_2. Titanite$_I$ forms thin trails parallel to S_2 and rarely occurs in clinopyroxene$_{II}$ layers.

Where S_2 is more developed epidote$_{II}$ (zoisite and clinozoisite) is in fine-grained crystals forming trails parallel to S_2 with clinopyroxene$_{II}$ and garnet$_{II}$.

Up to 1 cm-sized kinked pre-D_1 clinopyroxene porphyroclasts show SPO either parallel to S_1 or S_2. These porphyroclasts locally have opaque mineral exsolutions and are overgrown by rims of clinopyroxene$_{I/II}$ at the edges and along fractures. These rims do not contain opaque minerals, are optically continuous with the pre-D_1 clinopyroxene porphyroclasts, and form spikes parallel to S_2 foliation, suggesting that pre-D_1 clinopyroxene porphyroclasts partially recrystallised during D_2. The cores of pre-D_1 clinopyroxene porphyroclasts are locally replaced by Mg-chlorite along cleavages.

Pre-D_1 clinopyroxene porphyroclasts enclose pre-D_1 epidote crystals that also form aggregates wrapped by S_1; the core of these epidote crystals is Fe-rich, as suggested by high birefringence colours (Fig. 8b); epidote strain shadows are filled by Mg-chlorite$_I$ or $_{II}$. In more foliated rocks pre-D_1 clinopyroxene porphyroclasts are fractured within S_2, with mineral filling of clinopyroxene$_{II}$, garnet$_{II}$, and rare tremolite$_I$ (Fig. 8c). The high angle with S_2 and SPO of clinopyroxene$_{II}$ filling these fractures, suggest that they developed during D_2. These fractures are intersected by other fractures at a high angle with S_2 that are filled by coarse-grained euhedral epidote$_{II}$ crystals. Fractures cutting S_2 are filled by epidote$_{III}$, which is zoisite and clinozoisite where fractures intersect epidote$_I$ or epidote$_{II}$ and Fe-epidote where fractures intersect garnet, clinopyroxene$_{II}$, and Mg-chlorite$_{II}$ aggregates.

Rare post-D_2 tremolite$_{II}$ forms randomly oriented crystals overgrowing garnet and epidote layers. Rocks containing tremolite are the poorest in epidote.

Taking into account the described microstructural features, the following mineral growth - deformation relationships can be inferred in epidote-bearing rodingites:

- Pre-D_1 mineral relics: Cpx porphyroclasts, ± Ep (Fe-Ep);
- Syn-D_1: Ep$_I$, Cpx$_I$, MgChl$_I$, Grt$_I$;
- Syn-D_2: Ep$_{II}$, Cpx$_{II}$, MgChl$_{II}$, Ttn$_I$, ± Grt$_{II}$, ± Tr$_I$;
- Post-D_2: ± Ep$_{III}$, ± Tr$_{II}$.

Garnet-chlorite-clinopyroxene-bearing rodingites

Garnet-chlorite-clinopyroxene-bearing rodingites consist of: garnet (20 - 70%), Mg-chlorite (20 - 55%), clinopyroxene (≤ 50%), opaque minerals (≤ 5%), vesuvianite (≤ 10%).

These rocks are heterogeneously deformed and the dominant fabric can be the S_1 foliation, the crenulated S_1 with the newly forming variably differentiated S_2 crenulation cleavage, or the fully decrenulated continuous S_2 foliation.

S_1 is marked by garnet$_I$, Mg-chlorite$_I$, clinopyroxene$_I$, and rare prismatic vesuvianite$_I$. In samples where S_1 is pervasive, rare vesuvianite porphyroblasts, postdating S_1, enclose fine-grained garnet$_I$. Up to 1 cm-sized pre-D_1 clinopyroxene porphyroclasts have fractures filled mainly by fine-grained garnet$_I$ and/or clinopyroxene$_I$ showing complex relations: fractures filled by clinopyroxene$_I$ ± epidote$_I$ are intersected and displaced by fractures filled by garnet$_I$ ± Mg-chlorite$_I$ or garnet$_I$ fractures are intersected by clinopyroxene$_I$ fractures (Fig. 9a). Where fractures form a high angle with S_1, the mineral filling may be interpreted as syn-D_1; in other cases the relative chronology of mineral growth filling with respect to the deformation stages is not clear. Pre-D_1 clinopyroxene porphyroclasts are rimmed by garnet$_I$, which also grew in continuity along the S_1 films. Garnet$_I$ and minor clinopyroxene$_I$ + Mg-chlorite$_I$ also form aggregates, locally parallel to S_1, which could be pseudomorphs after pre-D_1 clinopyroxene porphyroclasts. The aggregates are affected by ductile boudinage with Mg-chlorite$_I$ in the necks. Two sets of conjugate micro-shear zones marked by Mg-chlorite$_{II}$ and rare vesuvianite$_{II}$ affect S_1 and kink Mg-chlorite$_I$.

Figure 9. Pre-Alpine and Alpine microstructures in Garnet-chlorite-clinopyroxene-bearing rodingites.

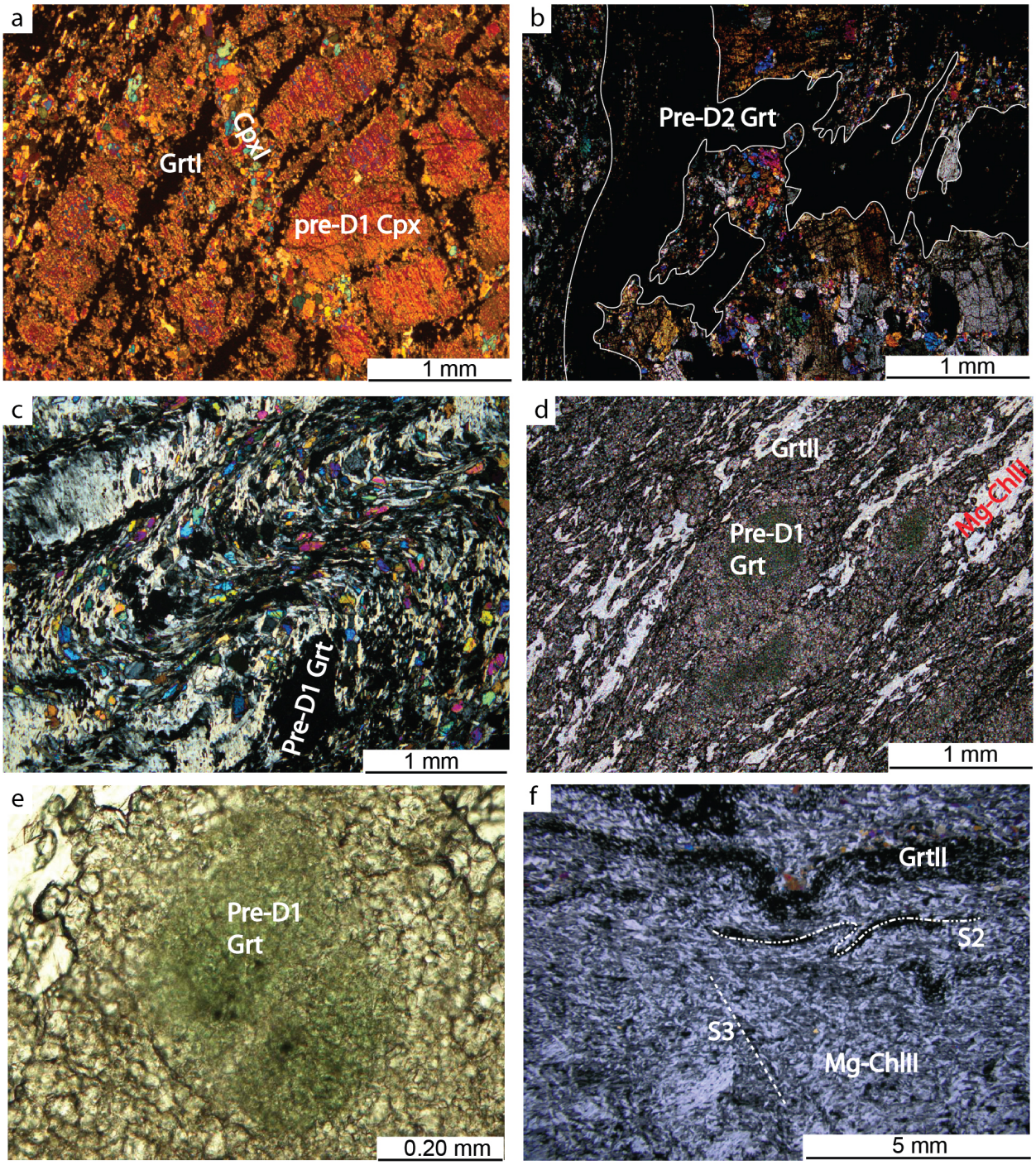

Mineral compositions related to microstructural sites are shown in Figs. 13 and 14 and in Tables 1 and 2. a) Pre-D_1 clinopyroxene porphyroclast transected by garnet$_I$-filled fractures and by clinopyroxene$_I$-filled fractures. Crossed polars. b) Microfolding and transposition along S_2 of a pre-D_2 garnet-vein; white line highlights vein margins; crossed polars. c) S_1 and the differentiated S_2 marked by garnet$_{I/II}$, Mg-chlorite$_{I/II}$, and clinopyroxene$_{I/II}$. An uvarovite-rich pre-D_1 garnet porphyroclast is preserved within the crenulated S_1; crossed polars. d) Uvarovite-rich garnet wrapped by S_2 foliation, marked by garnet$_{II}$, chlorite$_{II}$, and clinopyroxene$_{II}$; plane polarised light. e) Uvarovite-rich garnet porphyroclast with Cr-spinel (dark spots) preserved in the core: plane polarised light. f) Folded S_2 defined mainly by Mg-chlorite$_{II}$ and garnet$_{II}$-rich aggregates. Mg-chlorite$_{III}$ concentrates along the incipient S_3 differentiated cleavage; crossed polars.

Pre-D_2 garnet, clinopyroxene, and minor Mg-chlorite fill pre-D_2 veins, which are parallel to or folded and at a high angle with S_2 (Fig. 9b).

Where S_2 is only incipient, it is a spaced crenulation foliation with folded S_1 relicts within the S_2 films. S_1 and S_2 are marked by SPO of clinopyroxene$_I$ and $_{II}$ and garnet$_I$ and $_{II}$ and SPO and LPO of Mg-chlorite$_I$ and $_{II}$ respectively (Fig. 9c). Some clinopyroxene$_{II}$ grains show an internal foliation defined by opaque mineral that is slightly folded and in continuity with the external S_2, suggesting that these grains are syn-kinematic to S_2.

Locally S_1- or S_2-parallel garnet$_{I/II}$ aggregates wrap pre-D_1 garnet porphyroclasts, which have a green Cr-rich core and colourless rims recrystallised during D_1 or D_2 (Fig. 9d). The Cr-rich core may contain fine-grained Cr-rich spinel (Fig. 9e). When the pre-D_1 garnet aggregates are parallel to S_1 they are dismembered and folded by D_2.

Well-developed S_2 is marked by LPO and SPO of Mg-chlorite$_{II}$, garnet$_{II}$, clinopyroxene$_{II}$, and rare opaque minerals; clinopyroxene$_{II}$ forms layers parallel to S_2.

Pre-D_1 clinopyroxene porphyroclasts may also show SPO parallel to S_2. In this case garnet$_{II}$ crystallised in fractures at a low angle with clinopyroxene porphyroclast cleavages and in continuity with S_2. In wider fractures Mg-chlorite$_{II}$ forms crystals oriented at about 45° with respect to the fracture wall, suggesting wall-parallel shearing.

In D_2 microfolds, Mg-chlorite$_I$ forms aggregates of recrystallised decussate grains or is internally deformed. Mg-chlorite porphyroclasts are overgrown by garnet$_{II}$ along rims and cleavages and may be related to D_1 or pre-D_1 stages. Euhedral opaque minerals overgrow S_2.

Mg-chlorite$_{III}$ marks the incipient S_3 crenulation cleavage of locally asymmetric micro-folds (Fig. 9f). Rare Mg-chlorite$_{III}$ intersects S_2 films at low angle.

The microstructural features described above indicate the following mineral growth - deformation sequence:

- Pre-D_1 mineral phases: uvarovite-rich Grt, Cpx porphyroclasts, ± Cr-rich Spl, ± Mg-Chl
- Syn-D_1 or pre-D_2: Mg-Chl$_I$, Grt$_I$, ± Cpx$_I$, ± Ep$_I$, ± Ves$_I$, ± opaque minerals
- Syn-D_2 or post-D_1: Mg-Chl$_{II}$, Grt$_{II}$, Cpx$_{II}$, ± Ves$_{II}$, ± opaque minerals
- Syn-D_3: Mg-Chl$_{III}$.

Vesuvianite-bearing rodingites

Vesuvianite-bearing rodingites consist of: vesuvianite (25 - 55%); Mg-chlorite (10 - 55%); garnet (10 - 30%); clinopyroxene (5 - 20%).

S_2 foliation is marked by fine-grained garnet$_{II}$, SPO of zoned vesuvianite$_{II}$ and clinopyroxene$_{II}$, and LPO and SPO of Mg-chlorite$_{II}$ (Fig. 10a). S_2 is also marked by layers of different grain size and modal proportions of vesuvianite$_{II}$, clinopyroxene$_{II}$, or garnet$_{II}$ crystals with rare titanite$_I$ films and minor epidote$_I$.

Figure 10. Pre-Alpine and Alpine microstructures in vesuvianite-bearing rodingites.

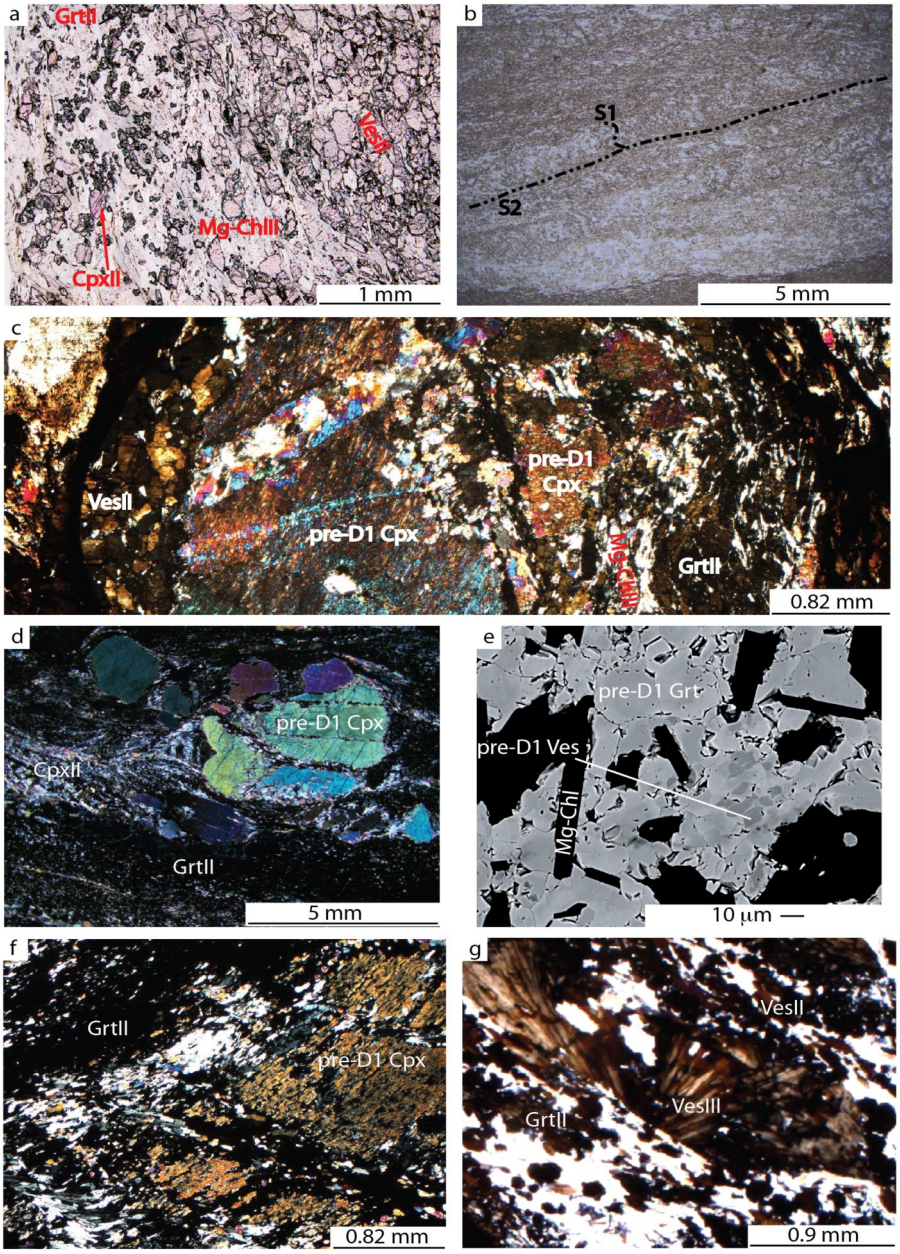

Mineral compositions related to microstructural sites are shown in Figs. 13, 14, and 15 and in Tables 1 and 2. a) Vesuvianite$_{II}$, garnet$_{II}$, Mg-chlorite$_{II}$, and minor clinopyroxene$_{II}$ marking S_2; plane polarised light. b) S_1 geometry preserved within S_2 lithons; stages of progressive enrichment of vesuvianite$_{II}$, Mg-chlorite$_{II}$, and garnet$_{II}$ are evident by variable thickness of S_2 films; plane polarised light. c) Clinopyroxene porphyroclast wrapped by and aligned along the S_2 foliation, marked by vesuvianite$_{II}$, garnet$_{II}$, Mg-chlorite$_{II}$, and clinopyroxene$_{II}$. New clinopyroxene crystallised at the rim and in fractures of the porphyroclast. Vesuvianite marking S_2 is zoned (see also Fig. 15); crossed polars. d) Fractured pre-D_1 clinopyroxene porphyroclast wrapped by S_2; Mg-chlorite$_{II}$ crystallised mainly in the strain shadows and Mg-chlorite$_{II}$ and garnet$_{II}$ filled the fractures. New clinopyroxene$_{II}$ is concentrated in the layer at the tip of the strain shadows; crossed polars. e) Pre-D_1 vesuvianite enclosed in the core of pre-D_1 garnet; backscattered SEM image. f) Pre-D_1 clinopyroxene porphyroclast replaced by garnet$_{II}$ and minor clinopyroxene$_{II}$ that grows along cleavages and fractures; crossed polars. g) Vesuvianite$_{III}$ overgrowing the S_2 foliation marked by vesuvianite$_{II}$, Mg-chlorite$_{II}$, and garnet$_{II}$; crossed polars.

Rare pre-D_2 clinopyroxene and Mg-chlorite are oblique to S_2 and locally form aggregates wrapped by S_2. Mg-chlorite$_I$ forms decussate aggregates of recrystallised grains within S_2 films, evidencing an S_1 relict foliation. S_1 is sporadically preserved between S_2 films

as a crenulated foliation (Fig. 10b) mainly marked by Mg-chlorite$_I$, vesuvianite$_I$, and garnet$_I$.

Mm-sized pre-D_1 clinopyroxene porphyroclasts are wrapped by S_2 and may show SPO parallel to S_2 (Figs. 10c, d). Minor epidote may be present as subhedral crystals at the pre-D_1 clinopyroxene porphyroclast rims. Very fine-grained opaque minerals are exsolved from the pre-D_1 clinopyroxene porphyroclast crystal lattice whereas the porphyroclast rims (clinopyroxene$_{II}$) do not contain opaque minerals. Strain shadows are filled by vesuvianite$_{II}$ and Mg-chlorite$_{II}$. Cr-rich pre-D_1 garnet porphyroclasts are wrapped by S_2 foliation and contain euhedral to subhedral crystals of pre-D_1 vesuvianite; therefore pre-D_1 garnet and vesuvianite are in contact by rational margins, suggesting textural equilibrium (Fig. 10e).

Garnet and clinopyroxene also grew along rims and fractures of clinopyroxene porphyroclasts (Fig. 10f). In some samples fractures occur in two sets, located at a low and high angle with respect to S_2; fractures in pre-D_1 clinopyroxene porphyroclasts at a high angle with S_2 can be interpreted as syn-D_2. Clinopyroxene$_{II}$-bearing fractures cut garnet$_{II}$ ± Mg-chlorite$_{II}$ and vesuvianite$_{II}$ filled fractures.

Vesuvianite$_{III}$ forms crystals or garbens that overgrow S_2 films (Fig. 10g). Mg-chlorite$_{III}$ fills veins intersecting S_2. Rare Mg-chlorite$_{III}$ marks an incipient S_3 axial plane foliation or intersects S_2 at a low angle.

Summarising, the following mineral growth-deformation relationships can be inferred:

- Pre-D_1 or pre-D_2 minerals: Cpx porphyroclasts, ± pre-D_1 Grt, ± pre-D_1 Ves
- syn-D_1 assemblage: Mg-Chl$_I$, ± Grt$_I$, ± Ves$_I$
- syn-D_2 assemblage: Ves$_{II}$, Mg-Chl$_{II}$, Cpx$_{II}$, Grt$_{II}$, ± Ttn$_I$, ± Ep$_I$
- syn-D_3 minerals: Mg-Chl$_{III}$, Ves$_{III}$.

Rodingite/serpentinite reaction rims:

The reaction rim of rodingites consists of clinopyroxene and chlorite bearing schists.

S_1 foliation is variably folded and mostly obliterated by the S_2 crenulation cleavage. S_1 is marked by a layering characterised by SPO and LPO of clinopyroxene$_I$ and chlorite$_I$ (Fig. 11a); minor opaque minerals may be scattered along S_1-parallel layers. Clinopyroxene$_I$ may define layers characterised by a remarkably variable grain size. Locally disharmonic folding of chlorite$_I$- and clinopyroxene$_I$-layers occurs. S_2 crenulation cleavage is marked by LPO and SPO of clinopyroxene$_{II}$, chlorite$_{II}$, and amphibole$_I$ (Fig. 11b). Chlorite$_{III}$ forms rare radial aggregates and randomly oriented amphibole$_{II}$ overgrew S_1 and S_2 or mimetically replaced clinopyroxene$_{II}$.

The above described microstructures suggest the following mineral growth-deformation relationships for the reaction rims:

- D_1: Chl$_I$, Cpx$_I$, opaque minerals
- D_2: Chl$_{II}$, Cpx$_{II}$, Amp$_I$
- Post-D_2: Amp$_{II}$, Chl$_{III}$

Figure 11. Alpine microstructures in rodingite reaction rims.

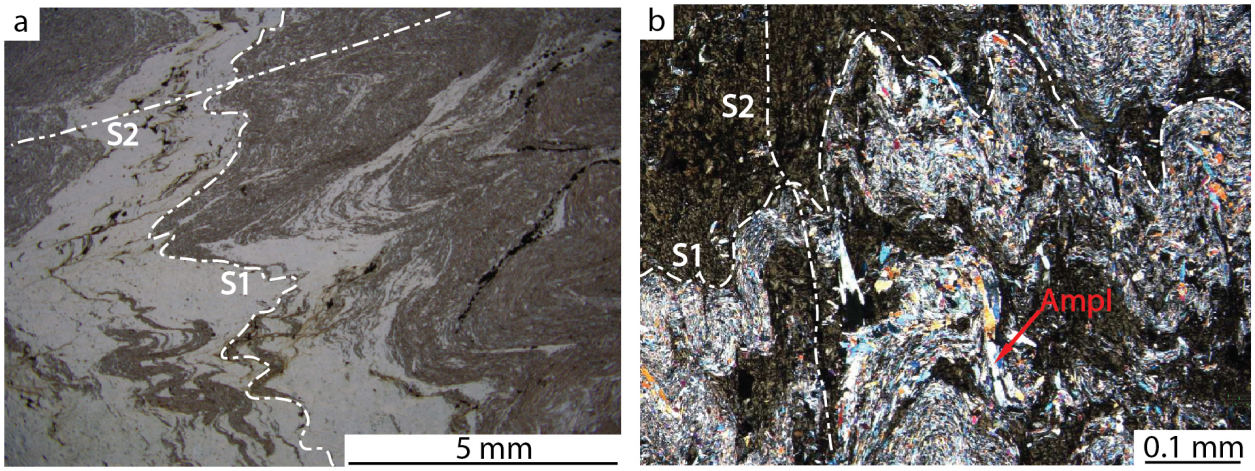

a) S_1 is marked by a mineral layering of alternating clinopyroxene$_I$ and chlorite$_I$, and is crenulated during D_2 deformation; plane polarised light. b) The S_1 foliation is crenulated during D_2. Clinopyroxene$_I$ and chlorite$_I$ mark S_1; the incipient differentiation of the S_2 crenulation foliation is highlighted by amphibole$_I$ crystals aligned with S_2; crossed polars.

Mineral chemistry

Mineral composition was measured with a Jeol, JXA-8200 electron microprobe (WDS, accelerating voltage of 15 kV, beam current of 15 nA) operating at the Department of Earth Sciences of Milano University. Natural silicates have been used as standards and the results were processed for matrix effects with a conventional ZAF procedure. Proportional formulae (see Tables 1 and 2) have been calculated on the basis of the following number of oxygen atoms: 6 for clinopyroxene, 12 for garnet, 12.5 for epidote, 28 for chlorite, and 76 for vesuvianite. Fe^{3+} was recalculated for garnet, epidote, and clinopyroxene on the basis of charge balance considerations.

Epidote

From core to rim, epidote marking S_2 foliation shows an early decrease (0.70 - 0.35 atoms per formula unit - a.p.f.u.) followed by an increase (0.35 - 0.55 a.p.f.u.) in Fe^{3+} associated with a corresponding Al variation from 2.30 to 2.60 and from 2.65 to 2.40 (a.p.f.u.), respectively (Fig. 12a). Mn is $\leq$ 0.02 a.p.f.u. and Ca ranges between 1.92 and 2.00 a.p.f.u. (Table 1). Epidote$_{II}$ in syn-D_2 strain shadows is the richest in Al.

Figure 12. Compositional variation of epidote and clinopyroxene.

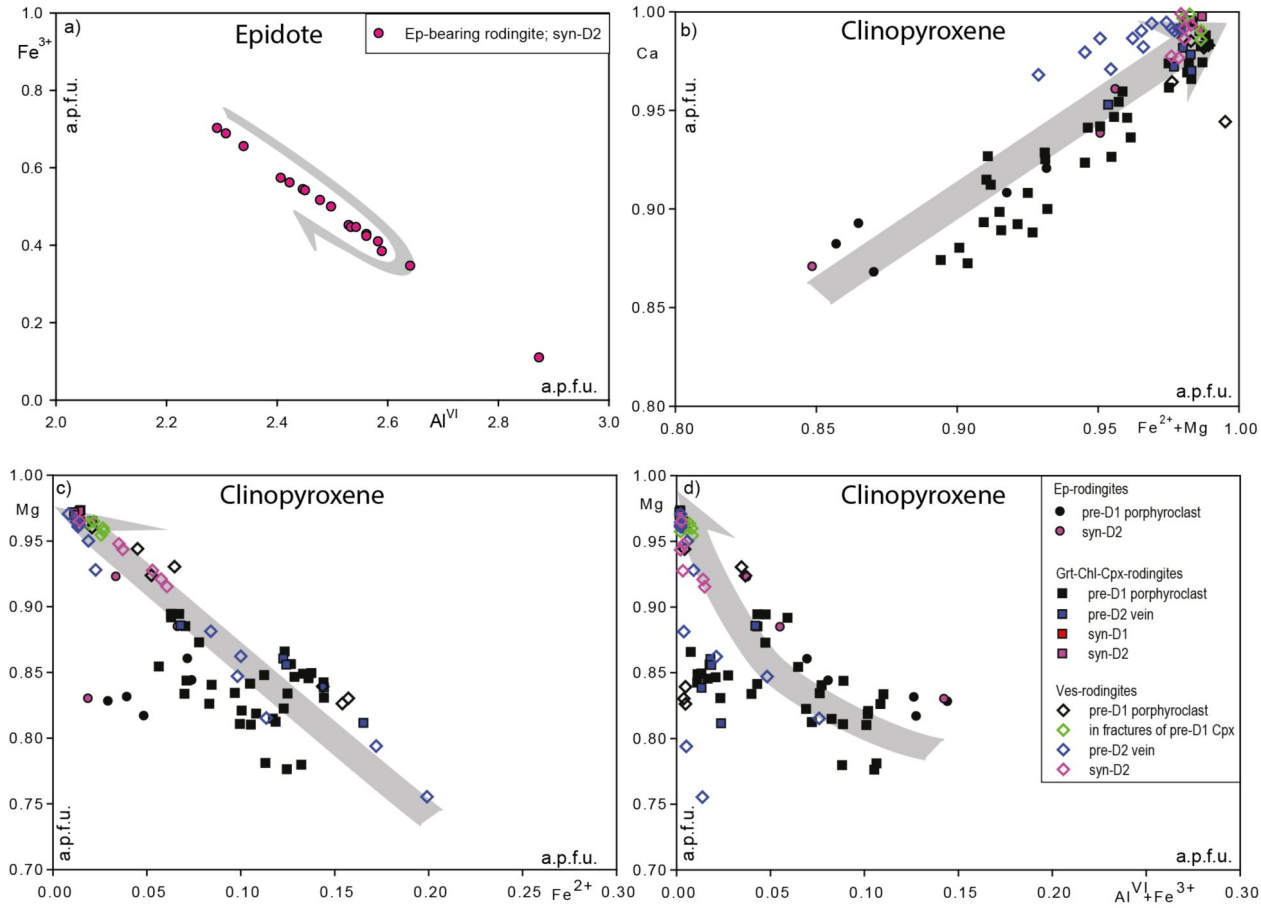

a) Compositional variations in Fe^{3+} vs. Al^{VI} from core to rim (grey arrow) of the $epidote_{II}$. From b) to d) composition of different generations of clinopyroxene in the three rodingite types: Ca vs. Fe^{2+}+Mg (b), Mg vs. Fe^{2+} (c), and Mg vs. Al^{VI} +Fe^{3+}(d) binary diagrams. The grey arrow indicates the chemical evolution from pre-Alpine to Alpine grains.

Epidote	Ep-rodingite			
	core synD2			rim synD2
SiO_2	37.69	38.26	38.41	38.57
Al_2O_3	24.32	26.57	28.83	27.43
TiO_2	0.07	0.07	0.06	0.05
Cr_2O_3	0.03	0.00	0.05	0.00
FeO^{tot}	11.42	8.61	5.94	7.79
MgO	0.04	0.06	0.08	0.10
NiO	0.01	0.00	0.00	0.02
MnO	0.04	0.20	0.15	0.21
CaO	22.38	23.83	24.17	23.68
Na_2O	0.00	0.01	0.01	0.00
K_2O	0.01	0.00	0.00	0.00
TOTAL	96.00	97.61	97.70	97.85
Si	3.01	2.98	2.97	2.99
Al^{IV}	0.00	0.02	0.03	0.01
Al^{VI}	2.29	2.42	2.59	2.50
Ti	0.00	0.00	0.00	0.00
Cr	0.00	0.00	0.00	0.00
Fe^{3+}	0.70	0.56	0.38	0.50
Fe^{2+}	0.06	0.00	0.00	0.01
Mg	0.00	0.01	0.01	0.01
Ni	0.00	0.00	0.00	0.00
Mn	0.00	0.01	0.01	0.01
Ca	1.92	1.99	2.00	1.97
Na	0.00	0.00	0.00	0.00
K	0.00	0.00	0.00	0.00
New FeO	0.93	0.00	0.00	0.00
New Fe_2O_3	11.66	9.57	6.60	8.55
New Total	97.17	98.57	98.36	98.71

Chlorite	Ep-rod.	Grt-Chl-Cpx-rodingite		Ves-rodingite	
	synD2	sinD1	synD2	synD2	postD2
SiO_2	29.77	31.64	29.04	31.90	31.18
Al_2O_3	21.03	19.56	21.01	19.13	20.11
TiO_2	0.00	0.00	0.00	0.00	0.01
Cr_2O_3	0.00	0.03	0.03	0.01	0.14
FeO^{tot}	5.44	1.76	12.96	1.82	1.99
MgO	29.80	32.95	25.12	32.73	32.07
NiO	0.14	0.15	0.12	0.20	0.16
MnO	0.16	0.19	0.11	0.17	0.15
CaO	0.06	0.06	0.07	0.06	0.38
Na_2O	0.00	0.00	0.00	0.02	0.04
K_2O	0.00	0.00	0.00	0.02	0.05
TOTAL	86.40	86.34	88.46	86.06	86.28
Si	5.71	5.95	5.65	6.02	5.89
Al^{tot}	4.75	4.34	4.82	4.26	4.48
Ti	0.00	0.00	0.00	0.00	0.00
Cr	0.00	0.00	0.01	0.00	0.02
Fe^{tot}	0.87	0.28	2.11	0.29	0.31
Mg	8.52	9.24	7.29	9.21	9.03
Ni	0.02	0.02	0.02	0.03	0.02
Mn	0.03	0.03	0.02	0.03	0.02
Ca	0.01	0.01	0.02	0.01	0.08
Na	0.00	0.00	0.00	0.01	0.02
K	0.00	0.00	0.00	0.01	0.01

Vesuvianite	Ves-rodingite			
	preD1	synD1	synD2	PostD2
SiO_2	37.47	37.42	37.27	37.21
Al_2O_3	17.71	19.79	16.16	19.14
TiO_2	1.15	0.05	0.22	0.03
Cr_2O_3	3.79	0.19	0.00	0.03
FeO^{tot}	1.46	1.79	3.77	3.35
MgO	0.03	1.44	2.67	1.21
NiO	0.00	0.00	0.02	0.03
MnO	0.09	0.36	0.22	0.03
CaO	36.80	35.71	36.02	36.13
Na_2O	0.01	0.01	0.00	0.02
K_2O	0.01	0.00	0.01	0.00
TOTAL	98.52	96.77	96.37	97.19
Si	18.19	18.13	18.19	18.02
Al^{tot}	10.13	11.31	9.30	10.93
Ti	0.42	0.02	0.08	0.01
Cr	1.45	0.07	0.00	0.01
Fe^{tot}	0.59	0.73	1.54	1.36
Mg	0.02	1.04	1.94	0.87
Ni	0.00	0.00	0.01	0.01
Mn	0.04	0.15	0.09	0.01
Ca	19.14	18.54	18.84	18.75
Na	0.01	0.01	0.00	0.02
K	0.01	0.00	0.00	0.00

Table 1. Selected analyses of epidote, chlorite, and vesuvianite.

Compositions of different generations of epidote, chlorite, and vesuvianite in the three rodingite types. Mineral formulae are calculated on the basis of 12.5, 28, and 76 oxygen atoms for epidote, chlorite, and vesuvianite respectively.

Clinopyroxene

Clinopyroxene is mainly a diopside with the core of pre-D_1 clinopyroxene porphyroclasts richer in augitic component (Morimoto, 1988). Pre-D_1 porphyroclasts have rims with a composition re-equilibrated with those of the rock matrix clinopyroxene. Pre-D_1 clinopyroxene porphyroclasts from vesuvianite-bearing rodingites have the lowest augitic content (Ca = 0.94-1.00 a.p.f.u.) whereas those from epidote-bearing rodingites have the lowest Ca content (0.87-0.92 a.p.f.u.). Clinopyroxene in pre-D_2 veins reach the highest Fe^{2+} content (in vesuvianite-bearing rodingite Fe^{2+} = 0.01 - 0.20; in garnet-chlorite-clinopyroxene-bearing rodingite Fe^{2+} = 0.07 - 0.17 a.p.f.u.) that decreases towards the clinopyroxene rim. In vesuvianite-bearing rodingites the composition of the pre-D_2 clinopyroxene rim is similar to that of the syn-D_2 clinopyroxene (Fe^{2+} = 0.01-0.06 a.p.f.u.). Clinopyroxene$_{II}$ and clinopyroxene$_{I}$ in garnet-chlorite-clinopyroxene-bearing rodingites have similar composition; Fe^{2+} ranges between 0.01 and 0.02 a.p.f.u.. Clinopyroxene$_{II}$ from epidote-bearing rodingites, has higher Fe^{2+} (0.02 and 0.07 a.p.f.u.) and lower and variable Ca (0.87 to 0.96 a.p.f.u.) content with respect to that one from the other types of rodingites, also due to complex zoning.

Clinopyroxene$_{I}$ and $_{II}$ composition overlaps that of the clinopyroxene$_{I}$ and $_{II}$ filling the fractures intersecting pre-D_1 clinopyroxene porphyroclasts (Fe^{2+} = 0.02 - 0.03 a.p.f.u.) supporting microstructural evidence that these fractures formed during D_1 and D_2 stages (Figs. 12b-d and Table 2).

Garnet	Ep-rod.	Grt-Chl-Cpx-rodingite			Ves-rodingite	
	SynD1	PreD1	SynD1	SynD2	PreD1	SynD2
SiO_2	38.72	37.46	37.70	37.56	37.19	38.52
Al_2O_3	20.82	8.30	8.93	8.64	7.52	14.48
TiO_2	0.22	0.08	0.24	0.14	0.09	0.23
Cr_2O_3	0.01	11.79	0.10	0.35	13.50	0.03
FeO^{tot}	15.90	6.92	17.18	17.23	5.91	10.71
MgO	2.15	0.06	0.11	0.16	0.03	0.20
NiO	0.01	0.03	0.02	0.03	0.00	0.03
MnO	1.33	0.40	0.37	0.43	0.34	0.72
CaO	21.63	34.67	34.69	34.41	34.51	34.47
Na_2O	0.02	0.00	0.01	0.01	0.02	0.00
K_2O	0.00	0.00	0.00	0.00	0.00	0.00
TOTAL	100.81	99.71	99.34	98.95	99.10	99.39
Si	2.97	3.00	3.00	3.00	3.00	3.00
Al^{tot}	1.88	0.78	0.84	0.81	0.72	1.33
Ti	0.01	0.00	0.01	0.01	0.01	0.01
Cr	0.00	0.75	0.01	0.02	0.86	0.00
Fe^{3+}	0.13	0.46	1.14	1.15	0.40	0.65
Fe^{2+}	0.89	0.00	0.00	0.00	0.00	0.04
Mg	0.25	0.01	0.01	0.02	0.00	0.02
Ni	0.00	0.00	0.00	0.00	0.00	0.00
Mn	0.09	0.03	0.03	0.03	0.02	0.05
Ca	1.78	2.97	2.96	2.95	2.99	2.88
Na	0.00	0.00	0.00	0.00	0.00	0.00
K	0.00	0.00	0.00	0.00	0.00	0.00
TotalCat	8.00	8.00	8.00	8.00	8.00	8.00
$NewFe_2O_3$	2.32	7.69	19.06	19.15	6.57	11.14
NewFeO	13.82	0.00	0.03	0.00	0.00	0.68
newTotal	101.04	100.48	101.25	100.87	99.76	100.50
End-members						
Uvarovite	0.00	0.37	0.00	0.01	0.43	0.00
Spessartine	0.03	0.01	0.01	0.01	0.01	0.02
Pyrope	0.08	0.00	0.00	0.00	0.00	0.00
Almandine	0.29	0.00	0.00	0.01	0.00	0.02
Grossular	0.53	0.38	0.41	0.39	0.35	0.62
Andradite	0.06	0.23	0.56	0.56	0.19	0.30

Pyroxene	Ep-rodingite	Grt-Chl-Cpx-rodingite				Ves-rodingite	
	PreD1	SynD2	PreD1	SynD1	SynD2	PreD1	SynD2
SiO_2	53.08	55.05	55.51	55.96	55.59	54.64	55.69
Al_2O_3	3.17	1.04	2.59	0.04	0.05	1.39	0.06
TiO_2	0.45	0.01	0.02	0.00	0.00	0.32	0.00
Cr_2O_3	0.10	0.00	0.08	0.02	0.02	0.00	0.00
FeO^{tot}	3.32	2.62	2.32	0.44	0.47	2.14	0.47
MgO	15.00	16.35	15.51	18.08	18.05	17.27	17.90
NiO	0.04	0.00	0.01	0.03	0.00	0.00	0.03
MnO	0.11	0.03	0.00	0.09	0.05	0.18	0.08
CaO	22.80	24.12	22.58	25.79	25.75	24.38	25.77
Na_2O	1.33	0.77	1.55	0.01	0.01	0.16	0.01
K_2O	0.01	0.00	0.00	0.00	0.00	0.00	0.00
TOTAL	99.41	99.99	100.16	100.46	99.99	100.49	100.01
Si	1.94	2.00	2.00	2.01	2.01	1.98	2.01
Al^{tot}	0.14	0.04	0.11	0.00	0.00	0.06	0.00
Ti	0.01	0.00	0.00	0.00	0.00	0.01	0.00
Cr	0.00	0.00	0.00	0.00	0.00	0.00	0.00
Fe^{3+}	0.05	0.01	0.00	0.00	0.00	0.00	0.00
Fe^{2+}	0.05	0.07	0.07	0.01	0.01	0.06	0.01
Mg	0.82	0.88	0.83	0.97	0.97	0.93	0.97
Ni	0.00	0.00	0.00	0.00	0.00	0.00	0.00
Mn	0.00	0.00	0.00	0.00	0.00	0.01	0.00
Ca	0.89	0.94	0.87	0.99	1.00	0.94	1.00
Na	0.09	0.05	0.11	0.00	0.00	0.01	0.00
K	0.00	0.00	0.00	0.00	0.00	0.00	0.00
TotalCat	4.00	4.00	4.00	4.00	4.00	4.00	4.00
$NewFe_2O_3$	1.59	2.19	2.32	0.44	0.47	2.14	0.47
NewFeO	1.92	0.47	0.00	0.00	0.00	0.00	0.00
newTotal	99.61	100.04	100.16	100.46	99.99	100.49	100.01
End-members							
Jd%	7.48	4.25	10.88	0.10	0.10	1.16	0.08
Ac%	1.92	1.17	0.00	0.00	0.00	0.00	0.00
Ca.FeTs%	2.77	0.00	0.12	0.03	0.02	0.00	0.00
Ca.TiTs%	1.24	0.04	0.04	0.01	0.01	0.89	0.01
Ca.Ts%	1.81	0.06	0.04	0.02	0.04	1.51	0.08
Woll%	41.50	46.87	43.63	50.10	50.13	46.21	50.31
En%	40.69	44.23	41.79	48.93	48.91	46.71	48.69
Fs%	2.59	3.38	3.51	0.81	0.78	3.52	0.84

Table 2. Selected analyses of garnet and clinopyroxene.

Compositions of different generations of garnet and clinopyroxene in the three rodingite types. Garnet end members are normalised to 1; sum of Al-schorlomite and morimotoite ≤ 0.02 (Locock, 2008). Clinopyroxene end members (Jd = jadeite; Ac = acmite; Ca.FeTs = Ca Fe-tschermakite; Ca.TiTs = Ca Ti-tschermakite; Ca.Ts = Ca-tschermakite; Woll = wollastonite; En = enstatite; Fs = ferrosilite) are expressed in per cent (Morimoto, 1988). Mineral formulae are calculated on the basis of 12 and 6 oxygen atoms for garnet and clinopyroxene respectively.

Garnet

In all rodingite types garnet mainly consists of andradite and grossular (Fig. 13 and Table 2), according to Locock (2008).

In the pre-D_1 garnet porphyroclasts of garnet-chlorite-clinopyroxene-bearing rodingite, uvarovite (37 - 45%), grossular (22 - 38%), and andradite (23 - 35%) are lower than in those from vesuvianite-bearing rodingite (uvarovite is up to 65%, grossular up to 68%, and andradite up to 37%). In vesuvianite-bearing rodingite pre-D_1 garnet has a composition grading to that of $garnet_{II}$ toward the rims (increasing in grossular and andradite and decreasing in uvarovite).

Figure 13. Composition of different generations of garnet

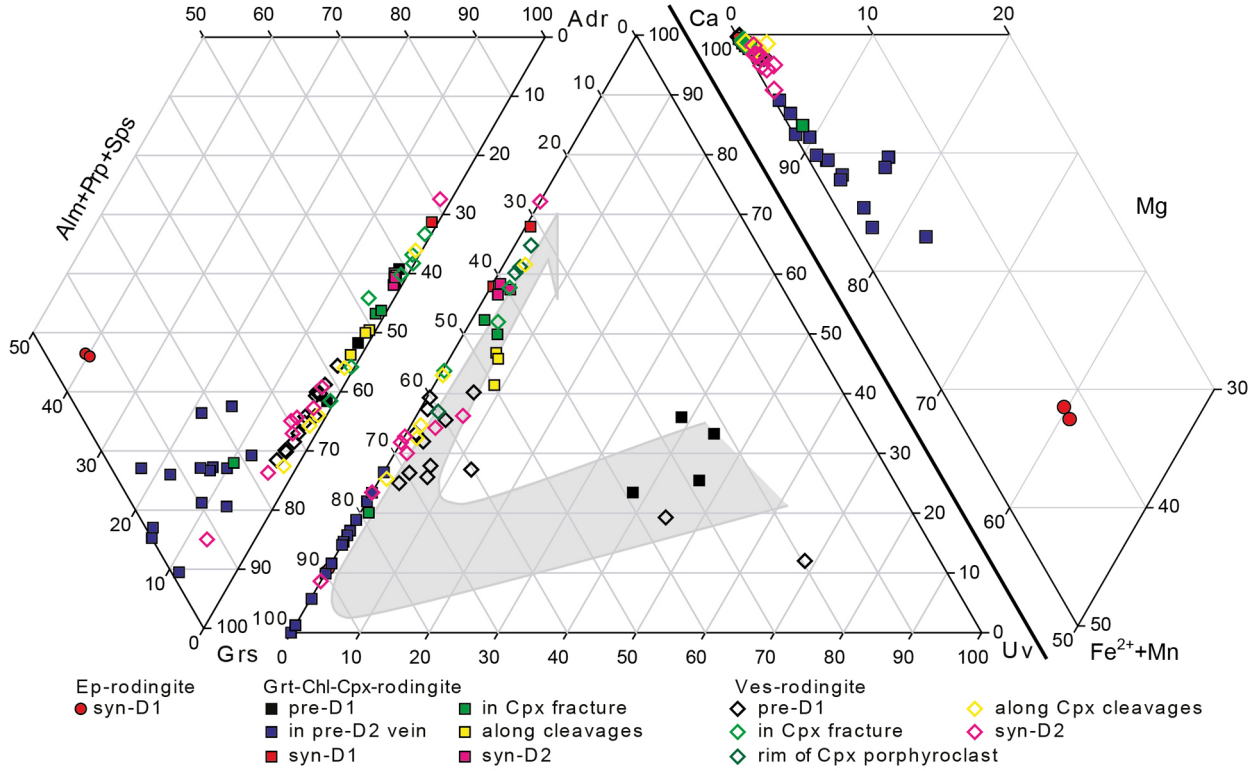

Composition of different generations of garnet in the three rodingite types is shown in almandine (Alm) + pyrope (Prp) + spessartine (Sps) vs. grossular (Grs) vs. andradite (Adr), grossular (Grs) vs. uvarovite (Uv) vs. andradite (Adr), and Ca vs. Fe^{2+}+Mn vs. Mg ternary diagrams. The grey arrow indicates the chemical evolution from pre-Alpine to Alpine generations of garnet.

Garnet in pre-D_2 veins has almandine (i.e. almandine - 5-16%, spessartine - 1-3%, pyrope - 0-5%, grossular - 59-87%, andradite - 0-21%) higher than all other garnet generations, with the exception of $garnet_I$ in epidote-bearing rodingite, where almandine is even higher (28-29%).

In garnet-chlorite-clinopyroxene-bearing rodingites $garnet_I$ shows higher andradite content (65 to 56% from core to rim) than $garnet_{II}$ (andradite = 54-57%). Uvarovite is between 1 and 3% in $garnet_{II}$ and < 1% in $garnet_I$. Garnet filling the clinopyroxene porphyroclast fractures shows lower content in andradite (47-50%) and higher in uvarovite (up to 5%) than $garnet_I$ and $_{II}$; in garnet along clinopyroxene porphyroclast cleavages, andradite (40-45%) is even lower, whereas uvarovite (6-8%) is higher.

In vesuvianite-bearing rodingites garnet grown at the rims, on cleavages, or in fractures of clinopyroxene porphyroclasts shows similar compositional ranges (andradite = 31 to 62%, andradite = 37 to 54% and andradite = 23 to 59% respectively) in which andradite increases toward the rim. In addition, garnet along the clinopyroxene cleavages also shows complex zoning patterns. $Garnet_{II}$ has heterogeneous composition with andradite ranging

between 7 and 66%, but clustering around 20 and 35%. Lower andradite contents (7-22%) occur where microstructures suggest a late garnet growth, whereas the highest contents (66%) are from rocks with the lowest modal amount of garnet and the highest of clinopyroxene.

H_2O content in garnet, which is common in rodingites, was not measured. Hydrogrossular described in the literature generally contains more that 5% of H_2O, and garnet from rodingites may reach about the 12% of H_2O (e.g. Rossman & Aines, 1991). Before Fe_2O_3 recalculation, we estimated contents in $H_2O < 2\%$ in our samples. In particular the most hydrated garnet are grown at the expenses of clinopyroxene porphyroclasts, especially in vesuvianite-bearing rodingites.

Chlorite

Chlorite (Table 1) is clinochlore with the sole exception of the chlorite in the pre-D_2 veins in garnet-chlorite-clinopyroxene-bearing rodingites that is pycnochlorite (Hey, 1954). In vesuvianite- and epidote-bearing rodingites, chlorite shows lower Fe content with respect to that in garnet-chlorite-clinopyroxene-bearing rodingites. Si varies between 5.63 and 6.11 a.p.f.u., Mg between 6.63 and 9.39 a.p.f.u., and Fe between 0.25 and 2.68 a.p.f.u..

Vesuvianite

In vesuvianite$_I$ Fe^{tot} is between 0.69 - 1.04 a.p.f.u. and Al^{tot} between 9.87 and 11.31 a.p.f.u. (Fig. 14a). In vesuvianite$_{II}$ Fe^{tot} increases (1.11 - 1.54 a.p.f.u.) and Al^{tot} decreases (9.69 - 9.25 a.p.f.u.) toward the rim (Fig. 14d). Fe^{tot} in vesuvianite growing along fractures in clinopyroxene porphyroclasts is 1.48 - 1.70 a.p.f.u. and Al^{tot} is 9.04 - 9.15 a.p.f.u. (Figs. 14a-c). Vesuvianite growing along clinopyroxene porphyroclast cleavages shows Al^{tot} contents of 7.81 - 8.93 a.p.f.u. and Fe^{tot} contents of 1.37 - 1.68 a.p.f.u.. Post-D_2 vesuvianite reaches the highest Al^{tot} (9.47 - 11.60 a.p.f.u.) and the lowest Fe^{tot} (0.52 - 1.55 a.p.f.u.) quantities (Fig. 14a).

Pre-D_1 vesuvianite has a very distinct composition characterised by higher amount in Ca (> 19 a.p.f.u.), Cr (1.45 - 1.90 a.p.f.u.), and Ti (0.42 - 0.50 a.p.f.u.) and much lower in Mg (0.02 - 0.03 a.p.f.u.) with respect to the later generations of vesuvianite, which have Ca lower than 19, Cr up to 0.14, Ti up to 0.25 and Mg varying between 0.87 and 2.04 a.p.f.u. (Figs. 14b-c). Only vesuvianite that grew on cleavages of pre-D_1 clinopyroxene porphyroclasts has very high Ti content (1.00 - 1.50 a.p.f.u.) provided by depletion in Ti of the clinopyroxene during vesuvianite growth that may occur at HP/UHP conditions, as accounted by their Fe^{tot}, Al^{tot}, and Mg contents, close to those of syn-D_2 vesuvianite (Figs. 14a-c). In addition, also vesuvianite filling fractures in clinopyroxene porphyroclasts shows higher Ti amount than the other syn-D_2 crystals (Fig. 14c).

Fe^{3+} in vesuvianite has been not recalculated because the total charge balance of the 13 Y sites does not satisfy the conditions reported by Gnos & Armbruster (2006). However, since the variation trends, from core to rim, of Fe^{tot} and Al^{tot} are opposite (Fig. 14d), we can infer that the Fe^{tot} increase is actually due to Fe^{3+}.

Based on the modal proportion (see microstructural analysis) and the composition of single mineral phases in the three rodingite groups, the following bulk rock compositions in oxide weight per cent have been inferred:

$SiO_2 \approx 43$; $CaO \approx 20$; $Al_2O_3 \approx 18$; $MgO \approx 10$; $FeO \approx 7$ in epidote-bearing rodingites.

$SiO_2 \approx 39$; $CaO \approx 21$; $Al_2O_3 \approx 14$; $MgO \approx 14$; $FeO \approx 10$ in garnet-chlorite-clinopyroxene-bearing rodingites.

$SiO_2 \approx 39$; $CaO \approx 24$; $Al_2O_3 \approx 16$; $MgO \approx 14$; $FeO \approx 5$ in vesuvianite-bearing rodingites.

Typically the sum of Na_2O, K_2O, TiO_2, Cr_2O_3, MnO is less than 2 weight per cent.

These compositions are comparable to those displayed by the rodingites of the Pfulwe region (Li *et al.*, 2008).

Figure 14. Compositional variation in vesuvianite.

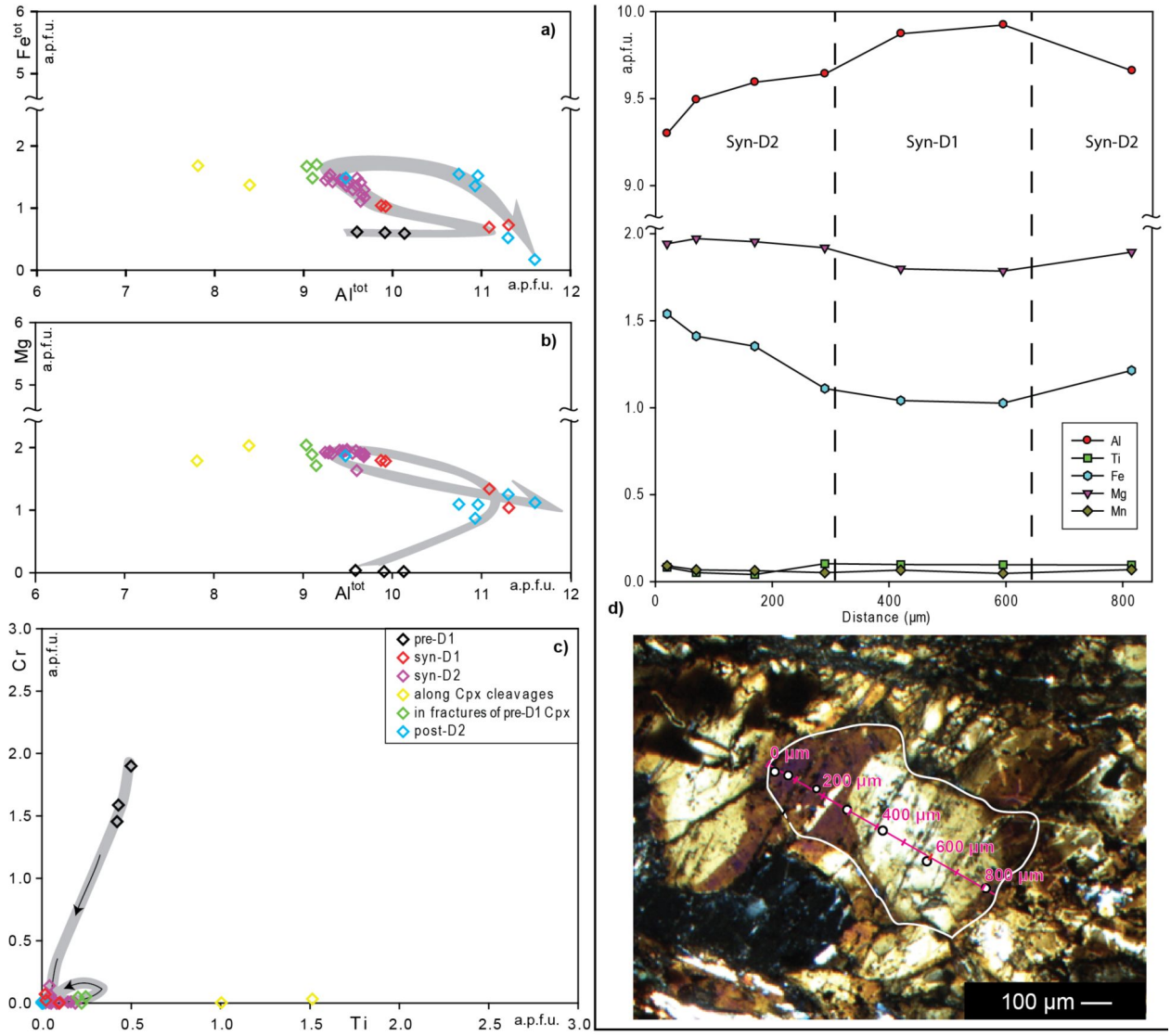

From a) to c) composition of different generations of vesuvianite is shown in Fe^{tot} vs. Al^{tot} (a), Mg vs. Al^{tot} (b), and Cr vs. Ti (c) binary diagrams. The grey arrow indicates the chemical evolution from pre-Alpine to late Alpine generations. d) Chemical zoning of a vesuvianite (I core and II rim) grain aligned with the S_2 foliation. White line highlights the grain edge and white circles indicate the position of analysed points. Crossed polars.

Conclusions

At Valtournanche four stages of ductile deformations have been detected in serpentinites and in the hosted rodingite dykes, in agreement with earlier structural reconstructions (Dal Piaz *et al.*, 1980). In serpentinites the first two stages are responsible for the development of S_1 and S_2 or the composite S_1/S_2 foliations, and the third one for a fold system and a differentiated S_3 crenulation cleavage or, locally, a disjunctive cleavage. S_1 and S_2 developed in eclogite facies conditions, whereas S_3 developed in epidote amphibolite facies conditions (Rebay *et al.*, 2012). The fourth stage is not associated with new mineral growth, it produces open folds, and is only rarely associated with a disjunctive cleavage. The full structural history is coherently recorded both in the rodingite dykes and in the surrounding serpentinite.

The mineralogical support of the S_2 differentiated foliation in serpentinites indicates PT conditions of 2.5 ± 0.3 GPa, for T of 600 ± 20 °C (Rebay *et al.*, 2012); its structurally coeval counterpart in rodingitised gabbro dykes is marked by the assemblages:

- Ep_{II}, Cpx_{II}, $MgChl_{II}$, Ttn_I, ± Grt_{II}, ± Tr_I in epidote-bearing rodingites;

- $MgChl_{II}$, Grt_{II}, Cpx_{II}, ± Ves_{II}, ± opaque minerals in garnet-chlorite-clinopyroxene-bearing rodingites;

- Ves_{II}, $Mg\text{-}Chl_{II}$, Cpx_{II}, Grt_{II}, ± Ttn_{I}, ± Ep_{I} in vesuvianite-bearing rodingites.

On the ground of structural correlation, these assemblages are interpreted to have formed under the same PT conditions estimated for S_2 in serpentinites at the transition between HP/UHP conditions.

The syn-D_3 mineral assemblages are instead interpreted as formed at P of ~0.7 GPa for T ~550°C, coherently with the inferred syn-D_3 PT conditions in serpentinites (Rebay *et al.*, 2012); the entire metamorphic evolution of the three rodingite types, associated with their syn-D_2 metamorphic assemblages, is shown on Fig. 15.

Mineral and structural relicts predating the S_1 foliation are related to the oceanic magmatic and metasomatic history. Cm-sized clinopyroxene porphyroclasts and fine grained Cr-rich spinel (e.g. Allan *et al.*, 1988) crystallised during the emplacement of the gabbro dykes, which are the rodingite protoliths, in the mantle rocks as already pointed out by previous authors (e.g. Dal Piaz, 1967). Moreover uvarovite-rich garnet and Ca- Cr-rich vesuvianite developed during the oceanic metasomatism responsible for the serpentinisation of the mantle rocks and the rodingitisation of the hosted gabbro dykes. Uvarovite-rich garnet is believed to form from the reaction between Cr-spinel and Ca-rich garnet assisted by the mobilisation of Cr by fluids circulation (e.g. Akizawa *et al.*, 2011; Mogessie & Rammlamair, 1994), or by reactions involving Cr-spinel, augitic pyroxene, and anorthitic plagioclase, both during ocean floor metasomatism. Being rich in Cr and Ti, pre-D_1 vesuvianite is consistent with being formed by the destabilisation of Cr-rich spinel during ocean floor metasomatism as well (Kobayashi & Kaneda, 2010); this is also supported by the full occupancy of the X+X' site (high Ca content), which is characteristic of low grade metamorphism (Gnos & Armbruster, 2006).

In general, since rodingitisation processes involve enrichment in CaO and MgO and depletion in SiO_2 of the mafic protoliths, the inferred bulk rock compositions from vesuvianite- to epidote-bearing rodingites suggest a decrease in oceanic metasomatism (see also Dubińska *et al.*, 2004; Schandl *et al.*, 1989). This is consistent with: a) pre-D_1 clinopyroxene porphyroclasts containing the lowest and highest amount of Ca in epidote- and vesuvianite-bearing rodingites respectively, which indicates a stronger chemical reworking of these porphyroclasts in vesuvianite-bearing rodingites; b) uvarovite-rich garnet and Ca- Cr-rich vesuvianite occurring only in garnet-chlorite-clinopyroxene- and vesuvianite-bearing rodingites.

Figure 15. Rodingite HP/UHP mineral assemblages and their PTdt path as deduced from hosting serpentinites

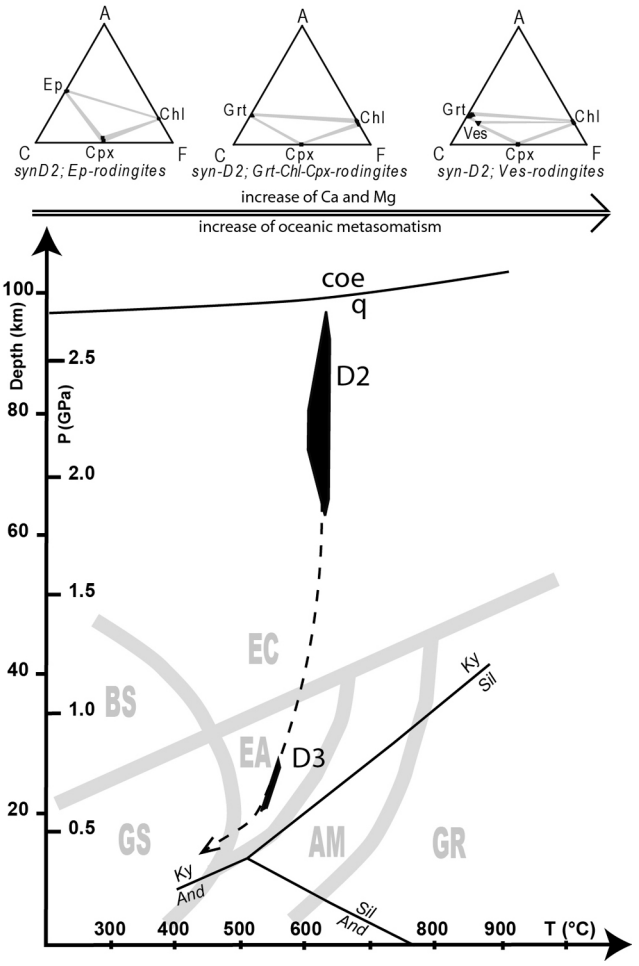

PTdt path (dashed line) of Alpine HP/UHP subduction-related (D_2) and LP exhumation-related (D_3) stages for serpentinites (Rebay *et al.*, 2012). The main HP/UHP mineral phases forming the assemblages of the three types of rodingites are shown in ACF projections, in which $A = (Al^{VI} + Fe^{3+})/2$; $C = Ca$; $F = Fe^{2+} + Mg + Mn$. In Vesuvianite-bearing rodingites garnet + chlorite + vesuvianite assemblage is the most common. The double black arrow indicates the increasing direction of Ca and Mg and the Piemonte-Ligurian oceanic metasomatism throughout the bulk compositional systems of the three rodingite types. Metamorphic facies are after Spear (1993).

On the other hand, different bulk rodingite composition may be also due to different composition of protoliths, but since a single rodingite boudin may consists of

different rodingite rock types (Fig. 6), we argue that the three different rodingite types most likely manifest a different progression in the rodingitisation process.

In all rodingite types, both pre-D_1 clinopyroxene and garnet porphyroclast rims show a chemical zoning with compositions that progressively approach those of the matrix clinopyroxene and garnet. This suggests a chemical reworking during the development of the S_2 foliation under the Alpine elcogite facies conditions. In this frame, the increase of andradite at the rim of pre-D_1 garnet may suggest an increase of oxygen fugacity during garnet transformation occurring during S_2 development.

The occurrence of Ca- Cr-rich pre-D_1 vesuvianite exclusively as inclusions in pre-D_1 uvarovite-rich garnet suggests that this phase is less resistant to recrystallisation during the Alpine subduction than uvarovite-rich garnet.

These data show that in rodingitised gabbro dykes at Valtournanche the pervasive structural and metamorphic imprint formed during the Alpine subduction. Subsequently these boudins have been poorly re-equilibrated both texturally and mineralogically during the Alpine exhumation under epidote amphibolite facies conditions.

Mineral relicts such as the core of pre-D_1 clinopyroxene and garnet porphyroclasts, Cr-rich spinel, and pre-D_1 vesuvianite are the only vestiges of the Piemonte-Ligurian oceanic history.

These data show that in Ca-rich systems vesuvianite can be stable also under HP/UHP conditions, as already suggested for the Pfulwe area of the Swiss portion of the ZSZ (Li *et al.*, 2008) and observed in jadeitites from Myanmar (Nyunt *et al.*, 2009). Finally, in the Valtournanche rodingites the detailed multiscale structural analysis made possible to discriminate HP/UHP-vesuvianite grains from oceanic relicts and late Alpine vesuvianite. This structural discrimination allowed individuating the significant variations in Cr-, Ti-, Ca-, and Mg-contents critical to detect vesuvianite grown in different metamorphic environments.

Acknowledgements

Aral I. Okay and Adrian F. Park provided constructive reviews of the paper. Curzio Malinverno provided the thin sections and Andrea Risplendente technical assistance at the microprobe. We acknowledge the support of PRIN 2008 “Tectonic trajectories of subducted lithosphere in the Alpine collisional orogen from structure, metamorphism and lithostratigraphy”. D.Z. acknowledges funding from the project: “Deformazione e metamorfismo delle ofioliti di alta pressione nelle Alpi Occidentali”, Università di Pavia.

References

Akizawa, N., Arai, S., Tamura, A. & Uesugi, J., 2011. Chromite and uvarovite in rodingite from the lowermost crust of Oman ophiolite: Cr mobility in hydrothermal condition. In: Japan Geoscience Union Meeting. Japan Geoscience Union, Makuhari, Chiba, Japan, SCG067-01.

Allan, J. F., Sack, R. O. & Batiza, R., 1988. Cr-rich spinels as petrogenetic indicators: MORB-type lavas from the Lamont seamount chain, eastern Pacific. American Mineralogist, 73: 741-753.

Amstutz, A., 1962. Notice puor une carte géologique de la Vallée de Cogne et de quelches autres espaces au Sud d'Aoste. Archives des Sciences de Genève, 15: 1-104.

Angiboust, S. & Agard, P., 2010. Initial water budget: The key to detaching large volumes of eclogitized oceanic crust along the subduction channel? Lithos, 120: 453–474. 10.1016/j.lithos.2010.09.007

Angiboust, S., Agard, P., Jolivet, L. & Beyssac, O., 2009. The Zermatt-Saas ophiolite: the largest (60-km wide) and deepest (c. 70–80 km) continuous slice of oceanic lithosphere detached from a subduction zone? Terra Nova, 21: 171-180. 10.1111/j.1365-3121.2009.00870.x

Austrheim, H. & Prestvik, T., 2008. Rodingitization and hydration of the oceanic lithosphere as developed in the Leka ophiolite, north–central Norway. Lithos, 104: 177-198. 10.1016/j.lithos.2007.12.006

Bach, W. & Klein, F., 2009. The petrology of seafloor rodingites: Insights from geochemical reaction path modeling. Lithos, 112: 103-117. 10.1016/j.lithos. 2008.10.022

Barnicoat, A. C. & Fry, N., 1986. High-pressure metamorphism of the Zermatt-Sass ophiolite, Switzerland. Journal of Geological Society London, 143: 607-618. 10.1144/gsjgs. 143.4.0607

Bearth, P., 1967. Die ophiolite der Zone von Zermatt-Saas Fee. Beiträge Geologische Karte Schweitz, 132: 1-130.

Bearth, P., 1976. Zur Gliederung der Bündnerschiefer in der Region von Zermatt. Eclogae Geologicae Helvetiae, 69: 149-161.

Beccaluva, L., Dal Piaz, G. V. & Macciotta, G., 1984. Transitional to normal MORB ophiolitic metabasites from the Zermatt-Saas, Combin and Antrona units, western Alps: implications for the paleogeografic evolution of the western Tethyan basin. Geologie en Mijnbouw, 63: 165-177.

Bortolami, G. & Dal Piaz, G. V., 1968. I filoni di gabbro rodingitici di Givoletto e Casellette nel massiccio ultrabasico di Lanzo (Torino). Bollettino della Società Geologica Italiana, 87(3): 479-490.

Bucher, K., Fazis, Y., de Capitani, C. & Grapes, R., 2005. Blueschists, eclogites, and decompression assemblages of the Zermatt-Saas ophiolite: High-pressure metamorphism of subducted Tethys lithosphere. American Mineralogist, 90: 821-835. 10.2138/am.2005.1718

Bucher, K. & Grapes, R., 2009. The eclogite-facies Allalin gabbro of the Zermatt-Saas ophiolite, Western Alps: a record of subduction zone hydration. Journal of Petrology, 50(8): 1405-1442. 10.1093/petrology/egp035

Caron, J. M., Polino, R., Pognante, U., Lombardo, B., Lardeaux, J. M., Lagabrielle, Y., Gosso, G. & Allenbach, B., 1984. Ou sont les sutures majeures dans les Alpes internes? (transversale Briançon-Torino). Memorie della Società Geologica Italiana, 29: 71-78.

Cartwright, I. & Barnicoat, A. C., 2002. Petrology, geochronology, and tectonics of shear zones in the Zermatt-Saas and Combin zones of the Western Alps. Journal of Metamorphic Geology, 20: 263-281. 10.1046/j. 0263-4929.2001.00366.x

Castelli, D., Rolfo, F. & Rossetti, P., 1995. Petrology of ore-bearing rodingite veins from the Balangero asbestos mine (Western Alps). In: Studies of metamorphic rocks and minerals of the Western Alps (edited by Lombardo, B.). Museo Regionale di Scienze Naturali, Torino, 13: 153-189.

Chinner, G. A. & Dixon, J. E., 1973. Some high pressure parageneses of the Allalin gabbro, Valais, Switzerland. Journal of Petrology, 14: 185-202. 10.1093/petrology/ 14.2.185

Coleman, R. G., 1967. Low-temperature reaction zones and alpine ultramafic rocks of California, Oregon and Washington. U.S. Geological Survey Bulletin, 1247: 1-49.

Cornelius, H. P., 1912. Petrographische Untersuchengen in den Bergen zwischen Septimer und Julierpass. Neues Jahrbuch für Mineralogie, Gelogie und Paläontologie, 35: 374-498.

Dal Piaz, G. V., 1965. La formazione mesozoica dei calcescisti con pietre verdi fra la Valsesia e la Valtournanche ed i suoi rapporti strutturali con il ricroprimento del Monte Rosa e con la Zona Sesia-Lanzo. Bollettino della Società Geologica Italiana, 84: 67-104.

Dal Piaz, G. V., 1967. Le "granatiti" (rodingiti L. S.) nelle serpentine delle Alpi occidentali italiane. Memorie della Società Geologica Italiana, 6: 267-313.

Dal Piaz, G. V., 1969. Filoni rodingitici e zone di reazione a bassa temperatura al contatto tettonico tra serpentine e rocce incassanti nelle Alpi Occidentali italiane. Rendiconti della Società Italiana di Mineralogia e Petrologia, 25: 263-316.

Dal Piaz, G. V., 1974. Le métamorphisme de haute pression et basse température dans l'évolution structurale du bassin ophiolitique alpino-apenninique. Schweizerische Mineralogische und Petrographische Mitteilungen, 54(2/3): 399-424.

Dal Piaz, G. V., 1999. The Austroalpine-Piedmont nappe stack and the puzzle of Alpine Tethys. In: 3rd workshop on Alpine geological studies. (edited by Gosso, G., Jadoul, F., Sella, M. & Spalla, M. I.). Memorie di Scienze Geologiche. Società Cooperativa Tipografica, Padova, Italy, 51: 155-176.

Dal Piaz, G. V., Di Battistini, G., Gosso, G. & Venturelli, G., 1980. Rodingitic gabbro dykes and rodingitic reaction zones in the upper Valtournanche-Breuil area, Piemonte ophiolite nappe, Italian Western Alps. Archives des Sciences de Genève, 33(2-3): 161-179.

Dal Piaz, G. V. & Ernst, W. G., 1978. Areal geology and petrology of eclogites and associated metabasites of the Piemonte ophiolite nappe, Breuil-St. Jacques area, Italian Western Alps. Tectonophysics, 51: 99-126. 10.1016/0040-1951(78)90053-7

Dal Piaz, G. V., Venturelli, G., Spadea, P. & Di Battistini, G., 1981. Geochemical features of metabasalts and metagabbros from the Piemonte ophiolite nappe, Italian Western Alps. Neues Jahrbuch für Mineralogie - Abhandlungen, 142(3): 248-269.

De Giusti, F., Dal Piaz, G. V., Schiavo, A., Massironi, M., Monopoli, B. & Bistacchi, A., 2003. Carta geotettonica della Valle d'Aosta. Memorie di Scienze Geologiche, 55: 129-149.

Dubińska, E., Bylina, P. & Kozłowsky, A., 2004. Garnets from lower Silesia rodingites: constraints from their chemistry. Polskie Towarzystwo Mineralogiczne – Prace Specjalne, 24: 135-139.

Ernst, W. G. & Dal Piaz, G. V., 1978. Mineral parageneses of eclogitic rocks and related mafic schists of the Piemonte ophiolite nappe, Breuil-St Jacques area, Italian Western Alps. American Mineralogist, 63: 621-640.

Ferrando, S., Frezzotti, M. L., Orione, P., Conte, R. C. & Compagnoni, R., 2010. Late-Alpine rodingitization in the Bellecombe meta-ophiolites (Aosta Valley, Italian Western Alps): evidence from mineral assemblages and serpentinization-derived H2-bearing brine. International Geology Review, 52(10-12): 1220-1243. 10.1080/00206810903557761

Fontana, E., Panseri, M. & Tartarotti, P., 2008. Oceanic relict textures in the Mount Avic serpentinets, Western Alps. Ofioliti, 33(2): 105-118.

Frezzotti, M. L., Selverstone, J., Sharp, Z. D. & Compagnoni, R., 2011. Carbonate dissolution during subduction revealed by diamond-bearing rocks from the Alps. Nature Geoscience, 4(10): 703-706. 10.1038/ngeo1246

Frost, B. R., 1975. Contact metamorphism of serpentinite, chloritic blackwall and rodingite at Paddy-Go-Easy Pass, Central Cascades, Washington. Journal of Petrology, 16(2): 272-313. 10.1093/petrology/16.2.272

Frost, B. R., Beard, J. S., McCaig, A. & Condliffe, E., 2008. The formation of micro-rodingites from IODP Hole U1309D: Key to understanding the process of serpentinization. Journal of Petrology, 49(9): 1579-1588. 10.1093/petrology/egn038

Gnos, E. & Armbruster, T., 2006. Relationship among metamorphic grade, vesuvianite "rod polytypism", and vesuvianite composition. American Mineralogist, 91: 862-870. 10.2138/am.2006.1973

Groppo, C., Beltrando, M. & Compagnoni, R., 2009. The P–T path of the ultra-high pressure Lago Di Cignana and adjoining high-pressure meta-ophiolitic units: insights into the evolution of the subducting Tethyan slab. Journal of Metamorphic Geology, 27: 207-231. 10.1111/j. 1525-1314.2009.00814.x

Hey, M. H., 1954. A new review of the chlorites. Mineralogical Magazine, 30: 277-292. 10.1180/minmag.1954.030.224.01

Hobbs, B. E., Ord, A., Spalla, M. I., Gosso, G. & Zucali, M., 2010. The interaction of deformation and metamorphic reactions. In: Advances in interpretation of geologic processes: Refinement of multi-scale data and itegration in numerical modelling (edited by Spalla, M. I., Marotta, A. M. & Gosso, G.). Geological Society of London Special Publications, 332: 189-222.

Honnorez, J. & Kirst, P., 1975. Petrology of rodingites from the equatorial Mid-Atlantic fracture zones and their geotectonic significance. Contributions to Mineralogy and Petrology, 49: 233-257. 10.1007/BF00376590

Kobayashi, S. & Kaneda, H., 2010. Rodingite with Ti- and Cr-rich vesuvianite from Sartuohai chromium deposit, Xinjiang, China. Journal of Mineralogical and Petrological Sciences, 105: 112-122. 10.2465/jmps.081224

Li, X. P., Rahn, M. & Bucher, K., 2004a. Metamorphic processes in rodingites of the Zermatt-Saas ophiolite. International Geology Review, 46: 28-51. 10.2747/0020-6814.46.1.28

Li, X. P., Rahn, M. & Bucher, K., 2004b. Serpentinites of the Zermatt-Saas ophiolite complex and their texture evolution. Journal of Metamorphic Geology, 22: 159-177. 10.1111/j. 1525-1314.2004.00503.x

Li, X. P., Rahn, M. & Bucher, K., 2008. Eclogite facies metarodingites – phase relations in the system SiO2-Al2O3-Fe2O3-FeO-MgO-CaO-CO2-H2O: an example from the Zermatt-Saas ophiolite. Journal of Metamorphic Geology, 26: 347-364. 10.1111/j.1525-1314.2008.00761.x

Locock, A. J., 2008. An Excel spreadsheet to recast analyses of garnet into end-member components, and a synopsis of the crystal chemistry of natural silicate garnets. Computers and Geosciences, 34: 1769-1780. 10.1016/j.cageo.2007.12.013

Martin, S., Rebay, G., Kienast, J. R. & Mevel, C., 2008. An ophiolitic palaeo-hydrothermal field metamorphosed in the eclogite-facies from the Italian western Alps, Saint Marcel valley. Ofioliti, 33: 49-63.

Martin, S. & Tartarotti, P., 1989. Polyphase HP metamorphism in the ophiolitic glaucophanites of the lower St. Marcel valley (Aosta, Italy). Ofioliti, 14(3): 135-156.

Messiga, B., Piccardo, G. B. & Ernst, W. G., 1983. High-pressure eo-alpine parageneses developed in magnesian metagabbros, Gruppo di Voltri, Western Liguria, Italy. Contributions to Mineralogy and Petrology, 83: 1-15. 10.1007/BF00373074

Mogessie, A. & Rammlamair, D., 1994. Occurrence of zoned uvarovite-grossular garnet in a rodingite from the Vumba Schist Belt, Botswana, Africa: implications for the origin of rodingites. Mineralogical Magazine, 58: 375-386. 10.1180/minmag.1994.058.392.03

Morimoto, N., 1988. Nomenclature of pyroxenes. Mineralogical Magazine, 52: 535-550. 10.1180/minmag.1988.052.367.15

Nicolas, A., 1966. Etude pétrochimique des Roches vertes et de leurs minéraux entre Dora Maïra et Grand Paradis. Le complexe Ophiolites-Schistes lustrés entre Dora Maïra et Grand Paradis. Tectonique et métamorphisme. Thése d'État, Nantes.

Nyunt,T.T., Theye, T. & Massonne, H.-J., 2009. Na-rich vesuvianite in jadeitite of the Tawmaw jade district, northern Myanmar. Periodico di Mineralogia, 78(3): 5-18.

O'Hanley, D. S., Schandl, E. S. & Wicks, F. J., 1992. The origin of rodingites from Cassiar, British Columbia, and their use to estimate T and P(H2O) during serpentinization. Geochimica et Cosmochimica Acta, 56: 97-108. 10.1016/0016-7037(92)90119-4

Palandri, J. L. & Reed, M. H., 2004. Geochemical models of metasomatism in ultramafic systems: Serpentinization, rodingitization, and sea floor carbonate chimney precipitation. Geochimica et Cosmochimica Acta, 68(5): 1115-1133. 10.1016/j.gca.2003.08.006

Panseri, M., Fontana, E. & Tartarotti, P., 2008. Evolution of rodingitic dykes: metasomatism and metamorphism in the Mount Avic serpentinites (Alpine ophiolites, Southern Aosta Valley). Ofioliti, 33(2): 165-185.

Passchier, C. W. & Trouw, R. A. J., 2005. Microtectonics. Springer, Berlin, Heidelberg, New York.

Pfeiffer, H. R., Colombi, A. & Ganguin, J., 1989. Zermatt-Saas and Antrona Zone: a petrogenetic and geochemical comparison of polyphase metamorphic ophiolites of the Western-Central Alps. Schweizerische Mineralogische und Petrographische Mitteilungen, 69: 217-236.

Piccardo, G. B., Messiga, B. & Cimmino, F., 1980. Antigoritic serpentinites and rodingites of the Voltri Massif; some petrological evidences for their evolutive history. Ofioliti, 5(1): 111-114.

Pitcher, W. S. & Flinn, G. W., 1965. Controls of Metamorphism. A symposium under the auspices of the Liverpool Geological Society. Oliver & Boyd, Edimburg, London.

Polino, R., Dal Piaz, G. V. & Gosso, G., 1990. Tectonic erosion at the Adria margin and accretionary processes for the Cretaceous orogeny of the Alps. Mémoires de la Société géologique de France, 156: 345-367.

Puga, E., Nieto, J. M., Díaz de Federico, A., Bodinier, J. L. & Morten, L., 1999. Petrology and metamorphic evolution of ultramafic rocks and dolerite dykes of the Betic Ophiolitic Association (Mulhacén Complex, SE Spain): evidence of eo-Alpine subduction following an ocean-floor metasomatic process. Lithos, 49: 23-56. 10.1016/S0024-4937(99)00035-3

Rebay, G., Spalla, M. I. & Zanoni, D., 2012. Interaction of deformation and metamorphism during subduction and exhumation of hydrated oceanic mantle: Isights from the Western Alps. Journal of Metamorphic Geology, 30: 687-702. 10.1111/j.1525-1314.2012.00990.x

Reddy, S. M., Wheeler, J. & Cliff, R. A., 1999. The geometry and timing of orogenic extension; an example from the Western Italian Alps. Journal of Metamorphic Geology, 17(5): 573-589. 10.1046/j.1525-1314.1999.00220.x

Reinecke, T., 1991. Very high pressure metamorphism and uplift of coesite-bearing metasediments from the Zermatt-Saas Zone, Western Alps. European Journal of Mineralogy, 10: 7-17.

Reinecke, T., 1998. Prograde high- to ultrahigh-pressure metamorphism and exhumation of oceanic sediments at Lago di Cignana, Zermatt-Saas Zone, Western Alps. Lithos, 42: 147-189. 10.1016/S0024-4937(97)00041-8

Rice, J. M., 1983. Metamorphism of rodingites: Part I. Phase relations in a portion of the system CaO-MgO-Al2O3-SiO2-CO2-H2O. American Journal of Science, 283(A): 121-150.

Ring, U., 1995. Horizontal contraction or horizontal extension? Heterogeneous late Eocene and early Oligocene general shearing during blueschist and greenschist facies metamorphism at the Pennine-Austroalpine boundary zone in the Western Alps. Geologische Rundschau, 84(4): 843-859. 10.1007/s005310050044

Rondolino, R., 1937. Sopra alcuni minerali della Valtournanche (Valle d'Aosta). Periodico di Mineralogia, 8: 53-56.

Rösli, U., Hoernes, S. & Köppel, V., 1991. Isotope data of metarodingites and associated rocks from the Lanzo and Bracco ophiolitic massif: indication on the evolution of the Alpino-type ultramafic-mafic complexes. Schweizerische Mineralogische und Petrographische Mitteilungen, 71: 125-141.

Rossman, G. R. & Aines, R. D., 1991. The hydrous components in garnets: Grossular-hydrogrossular. American Mineralogist, 76: 1153-1164.

Rubatto, D., 1998. Dating of pre-Alpine magmatism, Jurassic ophiolites and Alpine subductions in the Western Alps. Ph.D. thesis, Swiss Federal Institute of Technology, Zürich.

Schandl, E. S., O'Hanley, D. S. & Wicks, F. J., 1989. Rodingites in serpentinized ultramafic rocks of the Abitibi greenstone belt, Ontario. Canadian Mineralogist, 27(4): 579-591.

Spalla, M. I., Gosso, G., Marotta, A. M., Zucali, M. & Salvi, F., 2010. Analysis of natural tectonic systems coupled with numerical modelling of the polycyclic continental lithosphere of the Alps. International Geology Review, 52(10-12): 1268-1302. 10.1080/00206814.2010.482737

Spalla, M. I., Siletto, G. B., di Paola, S. & Gosso, G., 2000. The role of structural and metamorphic memory in the distinction of tectono-metamorphic units: the basement of the Como lake in the Southern Alps. Journal of Geodynamics, 30(1-2): 191-204. 10.1016/S0264-3707(99)00033-2

Spalla, M. I., Zucali, M., di Paola, S. & Gosso, G., 2005. A critical assestament of the tectono-thermal memory of rocks and definition of the tectono-metamorphic units: evidence from fabric and degree of metamorphic transformations. In: Deformation Mechanisms, Rheology and Tectonics: from Minerals to the Lithosphere (edited by Gapais, D., Brun, J. P. & Cobbold, P. R.). Geological Society, London, Special Publications, 243: 227-247.

Spear, F. S., 1993. Metamorphic phase equilibria and pressure-temperature-time paths. BookCrafters, Inc., Chelsea, Michigan.

Staub, R., 1915. Petrographische Untersuchungen im westlichen Berninagebirge. Zürcher & Furrer, Zürich.

Tsikouras, B., Karipi, S., Rigopoulos, I., Perraki, M., Pomonis, P. & Hatzipanagiotou, K., 2009. Geochemical processes and petrogenetic evolution of rodingite dykes in the ophiolite complex of Othrys (Central Greece). Lithos, 113: 540-554. 10.1016/j.lithos.2009.06.013

Turner, F. J. & Weiss, L. E., 1963. Structural analysis of metamorphic tectonites. MacGraw Hill, New York.

Van der Klauw, S. N. G. C., Reinecke, T. & Stöckhert, B., 1997. Exhumation of ultrahigh-pressure metamorphic oceanic crust from Lago di Cignana, Piemontese zone, Western Alps. Lithos, 41: 79-102. 10.1016/S0024-4937(97)82006-3

Weinschenk, E., 1894. Beiträge zur Petrographie der östlischen zentralalpen, speziell des Gross-Venedigerstokes. I. Über die Peridotite und die aus ihnen hervorgegangenen Serpentingesteine. Genetischer Zusammenhang derselben mit den sie begleitenden Minerallagerstätten. Abhandlung bayerische Akademie Wisseschaften, 18: 651-713.

Whitney, D. L. & Evans, B. W., 2010. Abbreviations for names of rock-forming minerals. American Mineralogist, 95: 185-187. 10.2138/am.2010.3371

Williams, P. F., 1985. Multiply deformed terrains - problems of correlation. Journal of Structural Geology, 7(3/4): 269-280. 10.1016/0191-8141(85)90035-5